The Compatibility of Tellurium with Austenitic Stainless Steels.

Ralph Leonard Joseph Lawson, M.Sc. Thesis, January, 1969.

SUMMARY

During the nuclear fission of plutonium fuels a number of volatile elements are produced that may corrode the surrounding cladding material. Of these elements, tellurium has been shown (67,68) to have a corrosive effect on stainless steels that are potential fuel cladding materials.

In the present research the effects of tellurium on a particular alloy, namely an A.I.S.I. 316L austenitic stainless steel were studied at temperature of 650°C and 750°C. Liquid tellurium was found to corrode the steel surface and reaction resulted in the formation of an intermediate phase. The corrosion embrittled the stainless steel with a consequent loss in mechanical properties as found by torsion tests at room and elevated temperature. The loss in mechanical properties increased with increased corrosion.

The degree of reaction was determined initially by the amount of tellurium in the compatibility couple. With a small amount of tellurium the reaction saturated and limited the corrosion, while a consistent, high concentration gradient stimulated the reaction which then depended upon tellurium diffusion through the intermediate phase.

The extent of the corrosion can be reduced by the preferential formation of a telluride, which will prevent liquid tellurium from wetting the alloy surface.

CONTENTS

1.0) INTRODUCTION.

During the fission process in a nuclear reactor certain elements are produced in the fuel by transmutation and radioactive decay. The elements that are produced can be represented in terms of the fission yield and mass number as illustrated in Fig.1. Under the prevailing condition of temperature and time during the operation of a reactor these elements may diffuse to, and react with, any cladding material used to contain the fuel. The United Kingdom Atomic Energy Authority and in particular, Dounreay Experimental Research Establishment are interested in the effects of volatile elements present in the plutonium fission product spectrum on the structure and properties of cladding materials proposed for the Prototype Fast Reactor.

1.1) The Prototype Fast Reactor

The third generation of commercial nuclear reactors will be based on a fast reactor principle and the need for, and design of, such a reactor has been discussed elsewhere (2-12). The only United Kingdom fast reactor at present is the experimental Dounreay Fast Reactor, which has a designed output of 60 M.W.T., but a prototype is under construction with a 600 M.W.T. designed output. Some of the features of the Prototype Fast Reactor are pertinent to the present work.

The Prototype Fast Reactor will be a liquid metal (sodium) cooled reactor designed with a coolant inlet temperature of 400 - 430°C and an outlet temperature of 500 - 600°C, while the maximum fuel cladding temperature will be 650°C. The initial fuel will be a solid solution of mixed oxide produced by co-precipitation and consisting of 85wt% uranium oxide and 15wt% plutonium oxide, eg. $(U,Pu)O_2$. The fuel will be of a sealed pin design in which a plenum will be provided for the accumulation of fission product gas as shown in Fig.2. To accommodate the volume increase associated with the accumulation of solid fission products and to defer expansion effects of retained fission gases a maximum bulk fuel density of approximately 85% will be realised.

1.2) Fuel Cladding Materials

The choice of cladding material is limited and depends upon the operating conditions of the fuel (12-21). To be suitable as a cladding, the material must meet the following requirements:-

i) It must protect the fuel from the corrosive effect of the coolant.

ii) It must prevent the escape of fission products.

iii) It must combine suitable nuclear, physical, mechanical and chemical properties under severe condition of temperature, stress, neutron and gamma radiation.

iv) It must not deform unduly, or fracture under the operating stress and requires a high creep strength, ultimate

tensile strength, a low coefficient of thermal expansion and good thermal conductivity.

Of the available metallic cladding materials the light metals and their alloys have low neutron capture cross-sections, below 1 barn, but the elevated temperature strength is limited and they do not resist corrosion by liquid sodium. Beryllium has a capture cross-section of 0.01 barns, but it is toxic and anisotropic with a limited ductility, which restricts cold working. The refractory metals resist attack by liquid sodium and combine this corrosion resistance with strength and creep ductility at high temperatures. Their relatively high neutron capture cross-sections can be tolerated to a degree in a fast flux system, especially if the section can be reduced. However, the cross-sections of tantalum and tungsten are high, of the order of 20 barns and with vanadium are comparatively expensive. Molybdenum will oxidise rapidly and is difficult to weld.

Stainless steels and nickel-base alloys have suitable high temperature strengths and resist corrosion by the coolant, but the nickel alloys can prove difficult to weld consistently and may contain cobalt, which results in a hard gamma radiation. A ductile alloy is required and this restricts the selection of a stainless steel to the austenitic grade, typical of which is the 18Cr-8Ni variety. The addition of molybdenum to this alloy improves the high temperature strength without any deleterious effect on the

ductility, provided the chromium and nickel contents are adjusted to retain the austenite structure.

Such an alloy is the A.I.S.I. 316 type which has a nominal composition of 17Cr-11Ni-2.5Mo. By vacuum melting and control of the carbon content to less than 0.03wt% any sensitisation, or embrittlement due to carbide and sigma phase precipitation respectively can be minimised and this results in the A.I.S.I. 316L grade of stainless steel. This alloy is readily available, comparatively economic and its technology understood. The neutron capture cross-section is of the order of 3 barns so that the section size must be minimised for neutron economy, even in a fast flux facility. However, the fuel is designed for a 10% burn-up of the fissionable atoms with a rating of 200-250 watts. grm^{-1}. and the resultant high temperature gradients restrict both the diameter of the fuel pin and the section of the cladding.

1.3) Compatibility with Tellurium

Little is known about the compatibility between the A.I.S.I. 316L stainless steel and one of the plutonium fission product elements, namely the group VI element tellurium, and the object of the present work was to study this compatibility in detail.

2.0) LITERATURE REVIEW.

2.1) The Stainless Steels

Austenitic stainless steels have been discussed in the literature with respect to their phase equilibria, physical, mechanical and nuclear properties. In particular the A.I.S.I. 316 and 316L grades have been studied with respect to precipitation and the effect of their structure on the high temperature properties of the materials.

2.1.1) Constitution of the Stainless Steels

Chromium and nickel are the two fundamental alloying additions made to iron to develop the stainless steels. By a suitable selection of the alloy content a range of steels can be produced which are conveniently classified by their structure as either ferritic, martensitic, austenitic, manganese-substituted austenitic, or precipitation hardening and which have a wide range of mechanical properties. The A.I.S.I. 316 and 316L steels belong to the austenitic group.

The effect of chromium on the structure of iron is to promote the formation of ferrite, while suppressing the austenite-phase field into a 'γ-loop' which extends upto approximately 12wt% Cr. (22,23). The sigma-phase is stable upto a temperature of the order of 820°C and decomposes by a eutectoid reaction at 520°C. This phase maybe present in the binary alloy with chromium

contents as low as 20wt%. The influence of carbon on the binary iron-chromium equilibrium diagram is to increase the limit of the 'γ-loop' to a higher chromium content and simultaneously widen the (α+γ) phase field. A limit is reached at 0.6wt% C when the 'γ-loop' extends to approximately 18wt% Cr and the (α+γ) phase field lies between 18wt% Cr and 24wt% Cr. Above 0.6wt% C the effect of this element is to produce free carbides of the type $(Fe,Cr)_3C$, $(Cr,Fe)_7C_3$ and $(Cr,Fe)_{23}C_6$ with an increasing chromium content (24).

Nickel extends the range of austenite stability in the binary iron-nickel system (22,23) and behaves in the opposite sense to chromium. The phase boundaries below 600°C are not precisely known because transformation at these temperatures is extremely slow.

The effects of both chromium and nickel on the structure of iron are shown in Fig.3a), b) and c), which are isothermal sections at 1200°C, 800°C and 650°C respectively of the Fe-Cr-Ni ternary equilibrium diagram drawn from the results of Schafmeister and Ergang(25) and Kinzel and Franks(26). The later work of Cook and Brown(27) did not indicate any radical change in the isothermal sections, but the sigma phase was shown to be present at lower chromium contents, Fig.4a) and b). This confirmed the results of Rees et al (28) and this discrepancy is probably a result of the low rate of transformation of these alloys, even after cold work. The

most recent work reported, that of Hattersley and Hume-Rothery (29) is in agreement with that of Price and Grant(30) at 1300°C and with that of Cook and Brown(27) at temperatures below 750°C. It appears that nickel will displace the sigma phase to a lower chromium content and higher temperatures, while decreasing the rate of transformation.

A number of other elements are present in the alloy both as a result of additions and as impurities in the steel making process. The latter residual elements have to be limited to control the mechanical and nuclear properties of the steel.

The effect of molybdenum on the structure of austenitic stainless steels was studied by Franks et al (31) and represented in terms of equilibrium phase diagrams at 1.75 to 2.25wt% Mo and 2.75 to 3.25wt% Mo. Recently, Pops(32) observed dispersion and age-hardening in alloys containing upto 7wt% Mo, but above 7wt% Mo the alloys were embrittled by chi-phase. Molybdenum has a similar effect to chromium in forming and stabilising the ferrite. Silicon stabilises the ferrite and has a greater effect than chromium in restricting the austenite phase field, while manganese and nitrogen have the opposite effect of promoting the austenite. Carbon when in solution behaves similarly to manganese and nitrogen, but out of solution the element preferentially forms carbides. The phosphorus and sulphur contents are minimised to reduce any intergranular micro-

fissuring in fully austenitic weld deposits, while the cobalt and boron contents are kept low because of their effects under irradiation. Cobalt can transmute in part to the Co^{60} isotope, while boron undergoes a (n,α) reaction to helium and lithium which may promote embrittlement of the alloy.

The effects of these minor elements can be related to the structure of the alloy in terms of their chromium and nickel equivalents. This was first suggested by Schaeffler(33) as a result of his work on the structure of weld deposits and later by Delong(34). The equivalent formulae suggested by Schaeffler(33) are as follows:-

The nickel equivalent = Ni + 30C + 0.5Mn.

The chromium equivalent = Cr + Mo + 1.55Si + 0.5Nb.

These empirical formulae introduced the concept of a balanced steel in which a given composition may retain a certain structure. If the nickel and chromium equivalents of the alloy used in the present work are calculated then the alloy (denoted by a cross) is seen to lie in the austenite phase field in Fig.3 at 1200°C, 800°C and 650°C. However, the later work of Cook and Brown(27) and illustrated in Fig.4, indicates that the alloy may lie on the δ-(γ+σ) phase boundary at a temperature of 650°C. Consequently, sigma phase may precipitate in the alloy at this temperature provided the transformation rate is high enough.

2.1.2) Precipitation of Carbide and Sigma Phase

Ageing of the solution treated A.I.S.I. 316L stainless steel for prolonged periods at elevated temperatures can result in precipitation of both carbide and sigma phase (35) with a consequent loss of toughness and impact strength. The sequence of precipitation will differ in cold worked and annealed steels. In the cold worked alloy subsequent precipitation will occur along slip planes as readily as in grain boundaries, but in the annealed condition precipitation will occur initially in the grain boundaries. The low carbon content of the alloy will minimise any precipitation and reduce the resultant degree of degradation in mechanical properties. Although the alloy lies on the $\gamma-(\gamma+\sigma)$ phase boundary at 650°C, the formation of sigma phase can be reduced by a high degree of metastability in the solution treated condition in which stress concentrations and ferrite are minimal.

The precipitation of the sigma phase in stainless steels has been the subject of various authors (36-40) and of a recent review by Hall and Algie(41). There appears to be an interdependence of carbide and sigma phase precipitation in that carbon in solution in the austenite will decrease the tendency for sigma phase formation, but precipitated carbide could reduce the threshold time for this phase. The carbide precipitates at a lower temperature than the sigma phase and consequently may induce the

precipitation of the latter. Talbot and Furman(38), however, found that sigma phase can form directly from the austenite, although precipitation is kinetically more favourable from ferrite and a cold worked matrix. Blenkinsop and Nutting(40) also found that carbide precipitation was not essential for nucleation of the sigma phase, which favoured precipitation within grain boundaries and at triple points in the austenite. These authors found that a solution temperature of 1300°C was necessary for the complete solution of the carbide and consequently, lower temperature of 1100°C, which are commonly employed for the solution treatment of the A.I.S.I. 316L alloy, will not retain all of the carbon in solution. Cold working and subsequent ageing of the lattice can result in transgranular sigma, associated with a hexagonal epsilon phase and precipitation at deformation twins with the crystallographic orientation relationship deduced by Blenkinsop and Nutting(40).

The precipitation of carbide in stainless steel has been discussed by Mahla(42), Lewis and Hattersley(43) and for the particular A.I.S.I. 316L alloy by Blenkinsop and Nutting(40). The morphology of the carbide varies according to the time and temperature of ageing from lamellar dendrites to stable geometric forms produced under equilibrium conditions. The carbide may precipitate in both twin boundaries and upon dislocations, oriented

with the lattice. In the A.I.S.I. 316L steel the complex cubic carbide which precipitates has a lattice parameter of 10.64°A and is of the type $M_{23}C_6$.

2.1.3) Mechanical and Physical Properties

The information in the literature on the mechanical and physical properties of types A.I.S.I. 316 and 316L stainless steels has been reviewed by Cope(35). Recently, the creep properties of these and other austenitic stainless steels have been discussed by various authors(44-47) in relation to their structure, because of their application for elevated temperature service, especially under irradiation. More than 12% of cold work at room temperature will produce deformation twins in the A.I.S.I. 316L alloy and the twin interfaces and intersections are suitable sites for the precipitation of carbide. Ageing results in such precipitation and reduces the amount of carbon in the matrix available for dislocation pinning. This can lead to an increase in the creep rate, as is found in practice.

2.1.4) Neutron Irradiation

The damage produced in metals and alloys by neutron irradiation has been discussed by Cottrell(48) and the effects of inert gas production reviewed by Blackburn(49). However, the effect of fast neutron irradiation on the properties of the A.I.S.I. 316L alloy has not been described specifically in the literature and

because of the difference in the flux spectrum it is probable that the mechanical properties after thermal neutron irradiation would differ to those produced in a fast flux facility.

Neutrons with energies greater than a few hundred electron volts damage stainless steel by the introduction of point defects, such as vacancies and interstitial atoms, into the lattice which harden the alloy. In addition, cascade collisions, which displace atoms from equilibrium may affect the rate and mechanism of atomic interchange as described by Bement(50). For example, the strain induced transformations, which occur below the MD temperature by cold work and results in the ε- or α'-phase influencing the strength and ductility, maybe altered by irradiation. However, elevated temperatures facilitate the return to equilibrium and consequently continuous exposure to a neutron flux produces a balance between the degree of damage and thermal relief.

Irradiation results in an increase in the yield stress and a decrease in the ductility of stainless steel, while the exact mechanism by which this occurs depends upon the temperature of exposure. Roy and Sully(51) suggested that above 700°C the loss of ductility in a 20Cr-25Ni-Nb alloy was due to the formation of helium bubbles at the alloy grain boundaries, but at 650°C the loss was a result of irradiation modified precipitation. Waddington(52) and Higgins and Roberts(53) detected the loss of ductility in

similar alloys and attributed it to the effect of irradiation on precipitation. A similar hardening effect in the A.I.S.I. 316 steel was found by Broomfield et al (54). Below 500°C the decrease in ductility of the steel was a result of the interaction between dislocations and irradiation induced point defects, but above 700°C the hardening was due to transmutation.

2.2) Corrosion by Liquid Metals

The literature contains several references on the corrosion of solid metals and alloys by liquid metals, but the majority describe problems which occur in joining processes, eg. soldering, coating techniques, eg. galvanising and tinning, embrittlement and season cracking phenomena (55-59). However, since 1958 attention has been drawn to the metallurgical and chemical problems associated with liquid metal coolants for thermal and fast reactors, and as a fuel-cladding bonding medium (60-65).

Corrosion of solid metals and alloys by liquid metals may be one, or more of the following types:-

i) the solution of the solid metal into the liquid metal by a) uniform solution,

b) intergranular solution, or penetration of the liquid metal into grain boundaries because of surface tension,

and c) crystalline facet development resulting from different solution rates in different crystallographic directions.

ii) diffusion of the liquid metal into the solid metal which may result in phase transformation by either transgranular, or intergranular diffusion.

iii) mass transfer due to either a composition, or a thermal gradient in a dynamic system.

iv) formation of an intermetallic compound at the surface of the solid.

v) selective leaching of a constituent of the alloy which may lead to void formation, or phase transformation.

vi) impurity reactions which may either stimulate, or suppress the reaction.

Not all of these types will occur in the specific case of the corrosion of austenitic stainless steels by liquid tellurium. Interference in the corrosion by impurity reactions vi) can be avoided by the design of a suitable experimental technique based upon an inert system. Mass transfer iii) as a result of either a composition, or a thermal gradient can be eliminated in a static system. The solution of the alloy i) into liquid tellurium would be limited by the low solubility, but a selective leaching v) of one of the constituent elements of the stainless steel may be more favourable. However, the chemistry of tellurium indicates the most probable type of corrosion to be one of intermetallic compound formation iv) with the degree of reaction depending upon the diffusion of

tellurium into the steel ii) either by a transgranular, or an intergranular path, or both. The diffusion into the austenite lattice will be limited by the solubility, but diffusion through a telluride(s) by the liquid phase may occur to stimulate reaction.

The diffusion mechanism was considered by Arkharov and Blankova(66) in the binary systems formed between iron-, nickel-, chromium-, manganese- and tellurium. The corrosion reaction was apparently due to diffusion by the liquid tellurium, while diffusion of the metal was only recorded at very high temperatures. In the Cr-Te system diffusion of chromium could not be detected at temperatures upto the melting point of the corrosion product, but manganese was found to diffuse at 600°C in the Mn-Te system.

2.2.1) Corrosion by Tellurium

The literature contains little reference to the corrosion of austenitic stainless steel by tellurium and none on the corrosion of the A.I.S.I. 316L grade.

Liquid tellurium corrodes 20Cr-25Ni-Nb stabilised stainless steel at 750°C, but Wells(67) suggested the extent of corrosion depends upon the concentration of the liquid metal. The product resulting from the corrosion by 0.5-1.0grm. of tellurium contained in a 0.4ins. diameter, 0.010ins. wall thickness tube for 400 hours was identified by x-ray diffraction as the iron telluride, ε-$FeTe_2$. Tube burst tests at pressures of 400-600lbs.ins^{-2} on

tubes containing upto 1grm. of tellurium at 750°C did not fail as a result of corrosion after exposure for 3,023 hours. However, the intermediate phase appears to embrittle the alloy and would be expected to affect its mechanical properties.

Horsley(68) studied the corrosion of 18Cr-8Ni-Ti stabilised stainless steel at 0.002mm. pressure of tellurium and 350°C for 100 hours exposure, and at 0.6mm. pressure, 500°C for 20 hours exposure. A surface scale similar to $MeTe_{1.4}$ formed, but this did not apparently affect the mechanical properties of the alloy on bend tests through 90°. The corrosion was reduced in a helium filled loop at one atmosphere pressure after exposure at 350°C for 100 hours. The inert argon atmosphere used by Wells(67) could also account for the lack of corrosion exhibited by the vapour phase in the system studied by this author.

The vapour pressure of tellurium can be calculated for a given temperature by the equations of Kubaschewski and Evans(69). The vapour pressures of liquid tellurium at 650°C and 750°C are 13.61mm. and 60.26mm. respectively. In a system containing argon at one atmosphere pressure and 25°C, the argon pressure would rise respectively at 650°C and 750°C to 3.1 and 3.4 atmosphere. Consequently, the partial pressure of tellurium at 650°C and 750°C in an inert system would be small, limiting the degree of corrosion by the vapour phase.

2.2.2) Constitution and Stability of the Tellurides

There is only a limited solubility between tellurium and the constituent elements of the A.I.S.I. 316L stainless steel. The phase equilibria reported in the literature is restricted to the binary transition metal-tellurium systems and to the range of stability of the compounds that form in each one. The liquidus in each system has yet to be determined. The phase equilibria is recorded in Table 1 and as a partial equilibrium diagram for the binary Fe-Te system in Fig.5. Table 1 illustrates how the compounds in each system form at similar tellurium compositions and that non-stoichiometry in the product of the stainless steel-tellurium reaction may allow substitution of other elements into the compound.

The stability of the transition metal tellurides is determined by the free energy of formation of the compound at the reaction temperature. For a general reaction of the following type;

$$A\langle Me\rangle + B\langle Te\rangle = C\langle MeTe\rangle \qquad (2.1)$$

the free energy of formation (ΔG) of the telluride can be calculated from the equation;

$$\Delta G_T = \Delta H_{298} + \int_{298}^{T} \Delta Cp.dT - T.\Delta S_{298} - T\int_{298}^{T} \frac{\Delta Cp}{T}.dT \qquad (2.2)$$

where ΔH is the heat of formation, ΔS the change in entropy and Cp the specific heat for a given temperature (T) and accounting for any transition in the reactants and products. The free energies of formation of the transition metal tellurides for the reactants in

their standard states have been calculated from the thermodynamic data of Mills(72), Kubaschewski and Evans(69) and Hultgren et al. (73). These free energies as a function of temperature are presented in Fig.6. The heat of formation at 298°K for the manganese telluride, $MnTe_2$ and the nickel telluride, $NiTe_{1.1}$ and the entropy at 298°K for the former were estimated. The chromium tellurides appear unstable above room temperature, while the manganese telluride (MnTe) is the most stable compound for the elements in their standard states. However, the transition metals are not in their standard states in the present work, but are in solution in the austenite. If Raoult's Law is assumed, the free energy of formation at a given temperature can be calculated from the Van't Hoff Isotherm, namely;

$$\Delta G = \Delta G^{\circ} + RT.\ln.\frac{a \text{ products}}{a \text{ reactants}} \qquad (2.3)$$

where the activity(a) of the product is assumed unity and that of the reactant equal to the mole. fraction. The free energies of formation for the elements in solution in the austenite are presented as the dashed lines in Fig.6. The β-iron telluride ($FeTe_{0.9}$) appears as stable as the manganese telluride ($MnTe_2$) at elevated temperatures. The effect of tellurium vapour can also be calculated from the Van't Hoff Isotherm (equation 2.3) if the activity of the product is assumed unity and that of tellurium equal to its vapour

pressure. At pressures below one atmosphere the telluride formed from the vapour phase would be less stable than that formed from liquid tellurium.

2.3) The Present Research

The literature survey illustrates that although research into the structure, properties and irradiation behaviour of austenitic stainless steel and liquid metal corrosion has been carried out, little study of the compatibility between A.I.S.I. 316L austenitic stainless steel and tellurium has been made. Consequently, the scope of the present research is as follows:-

i) an exploratory study of the compatibility to determine the nature and extent of the corrosion which will occur under the conditions of the Prototype Fast Reactor, neglecting the effect of a fast neutron flux, and

ii) a more fundamental study to determine the corrosion mechanism and the effect of reaction on the structure and mechanical properties of the alloy.

3.0) EXPERIMENTAL TECHNIQUE.

3.1) Design of the Compatibility Experiment

The design of an experimental technique for the compatibility study between A.I.S.I. 316L austenitic stainless steel and tellurium required an inert, static system to prevent oxidation and mass transfer by a composition gradient as discussed in the literature review (2.2). A consistent grade of stainless steel was essential for comparable results with regard to the extent of corrosion and its effect upon the mechanical properties of the alloy. Exposure at elevated temperatures for considerable periods of time required furnaces with a controlled high temperature zone and a minimum thermal gradient, preferably situated in an atmosphere with a constant temperature. The final technique developed is described below.

3.1.1) The Compatibility Couple

The A.I.S.I. 316L stainless steel was reactor grade material used in the form of tube. The composition and condition of the alloy is recorded in Table 2. This material realised one of the experimental requirements, namely that for a consistent grade of steel.

The second material used in the couple was tellurium and the relevant physical properties of this element are given in Table 3. The preliminary amount of tellurium used was 0.45grms per

compatibility couple based upon a 10% burn-up of the fuel (74), but any amount of tellurium could be added, the only restriction being upon the length of the alloy tube.

The exposure temperatures were 650°C and 750°C, based upon the reactor design, while initial periods of upto 10,000 hours were envisaged, the criterion here being the anticipated reactor life of a fuel pin.

3.1.2) Production of the Couple

The compatibility couples were produced by containing the required amount of fission product in the cladding tube under an atmosphere of purified argon, or in vacuo, to prevent the inclusion of oxygen in the system. Consequently, by exposing the couples vertically, both the liquid and vapour phase reactions could be studied. The production of the couple involved partial crimping of one end of the tube on a converted hydraulic press, addition of the fission product and purging of the system with argon at a slight positive pressure. With the argon purge maintained the crimp was completed and the end sealed by semi-automatic argon-arc welding. This weld was leak tested by immersion in liquid with an increased argon pressure. The other end of the tube was crimped at the required length under a pressure of 1,600 lbs.ins.$^{-2}$ to retain the inert atmosphere and sealed. This weld was leak tested. A welded compatibility couple is illustrated in Fig.7.

Control couples without tellurium were produced in a similar manner.

Each compatibility couple was sealed using an oxy-coal gas torch into a fused silica sheath evacuated to 1 μ pressure. The sheath was initially leak tested using a Pirani gauge and hydrogen test gas to ensure satisfactory seals. The sheathed couples were positioned vertically in silica jigs in electric resistance furnaces. Each furnace was made with three individual windings which controlled the temperature gradient along an 8inch. zone to $\pm 1^{\circ}C.ins.^{-1}$ maximum above and below the centre of the furnace. Two banks, each containing six furnaces were employed.

After exposure at temperature for the required time each compatibility couple was withdrawn from the furnace, air cooled to room temperature and examined by the technique described below. The couples were sectioned under alcohol to determine the soundness of the welds and whether a leak had developed.

3.2) A Preliminary Study of the Corrosion

3.2.1) Optical Microscopy

Compatibility couples were produced which contained 0.45 grms. of tellurium and tellurium rod. This rod was manufactured from the available crystals by melting under a vacuum of 1 μ in Pyrex tube of a suitable diameter, followed by uni-directional solidification. The diameter of the rod was selected to form a mechanical bond between the tellurium and cladding tube. Prior to

being sectioned, each couple was filled with a cold setting resin where necessary to protect the corroded bore. The mounted specimens were examined unetched and etched using the etchants given in Table 4. to determine the nature and extent of corrosion.

The penetration by liquid tellurium into the stainless steel was measured on transverse sections from similar positions in each couple. This ensured that every section was corroded by a similar amount of tellurium at a consistent temperature, even though each furnace had a low temperature gradient. The average of four readings on perpendicular ordinates was taken at a magnification of 200x with an error of $\pm 2.5\mu$. The outside surface of each couple was used as a reference point.

3.2.2) Micro-Indentation Hardness Testing

The applications, accuracy and factors which affect the accuracy of this hardness test have been discussed by Mott(75) and reviewed by Bückle(76). In an earlier paper, Bückle(77) described its use in the study of the diffusion behaviour of noble metal couples. The technique was used in the present work to follow the reaction between liquid tellurium and the austenitic stainless steel. Transverse sections of the corroded couples were mounted and mechanically polished, because electrolytic polishing removed the corroded layer.

A Leitz micro-indentation hardness testing machine was finally selected for the tests, because of the low inertia with

consequent reduction in susceptibility to vibration and the controlled loading rate of the instrument. The graticule was graduated to $\pm 0.5\mu$ and an estimation of $\pm 0.1\mu$ was possible. The instrument was calibrated to select a suitable load and contact time by testing at a constant load for various times and vice versa, until a consistent hardness was obtained. A load of 50grm. and a contact time of 10 seconds were found suitable in giving a hardness variation of 2-3 points V.H.N. at a hardness level of 250 V.H.N.

The Vickers Hardness Number by definition is;

$$\text{V.H.N.} = \frac{2.P.\sin\theta/2}{d^2} \text{ Kgrm.mm.}^{-2} \qquad (3.1)$$

where P is the load (Kgrms.), d the indentation diameter(mms) and θ the angle between opposite faces of the diamond pyramid indenter.

For a given indenter this becomes;

$$\text{V.H.N.} = K.\frac{P}{d^2} \qquad (3.2)$$

where K is a constant equal to $2.\sin\theta/2$.

$$\therefore \frac{d(\text{V.H.N.})}{dP} = \frac{K}{d^2} = \frac{\text{V.H.N.}}{P} \qquad (3.3)$$

and for a loading error of ΔP, the error in hardness is $\Delta(\text{V.H.N.})$, or

$$\frac{\Delta(\text{V.H.N.})}{\text{V.H.N.}} = \frac{\Delta P}{P} \qquad (3.4)$$

Consequently, for a low error in loading a high load is required. If the loading error, P_o, is independent of the load, P, equation (3.2) becomes;

$$V.H.N. = \frac{K(P + P_o)}{d^2} \tag{3.5}$$

$$\text{and } d^2 = K_1(P + P_o) \tag{3.6}$$

where K_1 is a constant when the hardness is independent of the load. The transgranular hardness of a control couple is given below for several different applied loads.

Load (grms)	Load ($\log_{10}$)	Indentation Diameter (μ)	Diameter ($\log_{10}$)	Diameter^2	V.H.N.
15	1.1761	10.8	1.0334	116.6	238
25	1.3979	12.9	1.1106	166.4	279
50	1.6990	18.9	1.2765	357.2	260
100	2.0000	27.75	1.4435	770.0	241

The square of the indentation diameter is a linear function of the load as given by equation (3.6) and there is a negligible loading error.

The hardness, as shown above, varies with the load and can be represented by the Meyer equation;

$$P = a.d^n \tag{3.7}$$

where P and d were given previously, a is a constant and n the exponent which is equal to two for a work hardened material. By substitution, the Vickers hardness, equation (3.1) becomes;

$$V.H.N. = 2.\sin\theta/2.a.d^{n-2} \tag{3.8}$$

The value of the exponent n was found to be 1.85 from the logarithm of the load and the indentation diameter. Consequently the hardness depends upon both the load, below 50grm and upon the material condition. Therefore, the hardness determined is not an absolute value, especially at an applied load of less than 50grm., but the values should be comparable on each section.

3.3) A Detailed Study of the Corrosion

3.3.1) X-Ray Diffraction

The corrosion of stainless steel by liquid tellurium resulted in an intermediate phase and the structure of this product was determined by x-ray diffraction. The effect of tellurium was to embrittle the alloy and this brittleness facilitated the extraction of the product from the bore of the corroded couples. The extracted samples were reduced to powder, stress-relieved at ~100°C under vacuum and analysed in a Debye-Scherrer type of camera using a Bradley-Jay technique.

To simplify the analysis of the powder patterns, x-ray diffraction patterns were taken of the solution treated stainless steel and chemically pure tellurium for comparison, using CoK_{α} radiation and an iron filter.

3.3.2) Electron Microscopy

Electron microscopy was used to determine the nature and morphology of the reaction product that formed between liquid tellurium and the cladding material. The geometry of the corroded

couples proved to be a problem in specimen preparation and surface replication was the most successful technique. However, even replicas were difficult to strip from the 0.015ins. sections without tearing the film at the section-mount interface. At the interface a small gap developed because of contraction of the mounting medium and the deposited film keyed into this gap. Extraction facilitated the stripping of the replicas except in the case of fractographs where the uneveness of the fracture face hindered removal. The replica area was increased by using flat, longitudinal sections of the corroded couples and mechanically polishing away the stainless steel in stages towards the corroded bore. This was useful for identifying the precipitates in the cladding material and inherent to the structure of the alloy.

3.3.3) Electron Probe Microanalysis

A Cambridge Microscan was used to determine the change in composition of the A.I.S.I. 316L austenitic stainless steel which occurred after corrosion by liquid tellurium across the reaction interface. The analysis was achieved in two ways. Initially the specimens were scanned by the electron beam on a raster and the intensity of the emitted, characteristic radiation for the element analysed traced on a pen recorder. This gave the comprehensive distribution of the element across the section of the corroded couple. The analysis of particular features illustrated by this

trace was then repeated by a system of point counting for each of the elements of interest. The trace for each element analysed was superimposed to obtain the change in composition with distance across the reaction interface. This allowed the composition to be studied as a function of the degree of corrosion for every couple.

Each of the 'raw' analyses, or k_A values, had to be corrected for the effects of atomic number, fluorescence and absorption of the excited radiation in the matrix. The method involved calculation by an iteration which is suitable for computer correction, especially in the current analysis when upto six elements were of interest. A programme based on correction procedures by Duncumb, Philibert, Bishop and Dacas(78) was available and this was used for the conversion of the k_A value to accurate weight percentage.

Verification of the Computer Programme

In order to verify the correction procedure as far as was possible for the present work a series of iron tellurides were synthesised and analysed chemically by a method given in Vogel(79). These results were then compared with the corrected analyses found by electron probe microanalysis. The iron tellurides were selected because iron is the major constituent of the stainless steel and appeared to be active in the formation of an intermetallic compound in the corroded couple as shown in the literature survey (2.2.1). Synthesis of the compounds was essential because these tellurides

were not commercially available.

The iron tellurides were synthesised from the chemically pure, powder constituents by a technique involving vacuum fusion. The powders in the correct proportion were intimately mixed, sealed in inert silica capsules under a pressure of $<1\mu$ and diffused for long periods at elevated temperatures. Small melts were made of approximately 20grm. to facilitate diffusion and reduce segregation. This was also realised by removing the melt from time to time during diffusion and grinding to a powder before re-sealing and exposing at temperature. The tellurides manufactured had the following theoretical compositions;

Phase	Formula	Atomic% Te	Weight% Te
β	$FeTe_{0.9}$	47.40	67.32
γ	$FeTe_{1.1}$	52.50	71.63
δ	$FeTe_{1.5}$	60.00	77.41
ϵ	$FeTe_2$	67.00	82.24

and the heat treatments given to each compound were as follows;

β	diffused	16	hours	at	900°C	and	2x168	hours	at	500°C;	quenched	to	25°C.
γ	-	16	-	-	900°C	-	2x168	-	-	750°C;	-	-	25°C.
δ	-	16	-	-	900°C	-	2x168	-	-	650°C;	-	-	25°C.
ϵ	-	16	-	-	900°C	-	2x168	-	-	400°C;	-	-	25°C.

These compounds and their ranges of stability have been discussed in the literature survey (2.2.2) and illustrated in Fig.5. The structure of the compounds was determined by x-ray diffraction (3.3.1 and 5.1.2) of powder samples and the patterns compared with the interplanar spacings given in the A.S.T.M. Card Index (70).

The patterns correlated except that for the γ-iron telluride which was of low contrast, but this compound was known to be segregated after examination under the optical and polarised light microscopes and by the variation in the chemical analysis of various samples.

The compositions of the tellurides determined by chemical and electron probe microanalysis were as follows;

	Phase	Melt Composition	Chemical Analysis	E.P.M.A.
β	Te wt%	67.32	67.03(-0.29)*	66.34(-0.98)
	Fe wt%	32.68	33.65(+0.97)	33.45(+0.77)
γ	Te wt%	71.63	segregated	
	Fe wt%	28.37		
δ	Te wt%	77.41	77.99(+0.58)	77.51(+0.10)
	Fe wt%	22.59	21.40(-1.19)	22.86(+0.27)
ε	Te wt%	82.24	82.06(-0.18)	81.81(-0.43)
	Fe wt%	17.76	17.41(-0.35)	18.47(+0.71)

* Error compared with the melt composition given in brackets.

Except for the iron content of the δ-phase the results were in good agreement as shown in Fig.8.

Limitations of the Analysis

There were two limitations of electron probe microanalysis which applied to the present work. The first was that in the analysis of corroded couples a low magnification was required to survey the whole of the reaction zone, while a high magnification was necessary to study areas in detail. Exact correlation of the

positions of each area was difficult. Secondly, precipitates whose size was less than the diameter of the electron beam could not be accurately analysed and in this case the results were average values for the selected area. This appears to apply in the present research where a telluride less than 1μ in length was resolved by electron microscopy (5.1.3).

3.4) Determination of Mechanical Properties

3.4.1) Torsion Testing

The corrosion of the A.I.S.I. 316L steel by liquid tellurium produced a change in the structure of the steel at the reaction interface which was related to the mechanical properties of the alloy at room and elevated temperature by torsion testing. Torsion testing was used in preference to the tensile test, because of the problems encountered in gripping the corroded specimens, particularly at high temperatures. A set of grips were designed, suitable for torsion testing at room and elevated temperature. The torsion testing machine used for the present work has been described in detail by Dragan(80) and will not be repeated here. Mechanical testing at elevated temperature was accomplished by inserting the gauge length in an induction coil and surrounding the specimen by an inert atmosphere of argon to prevent oxidation. The temperature was measured by a thermo-couple spot-welded to the centre of the gauge length and controlled by a saturable reactor connected to the supply.

Stress-Strain Relationships

The torsion test has been used for assessing the hot workability of metals and alloys. In this context it has been described by Hodierne(81), Hughes(82) and Nicholson(83) and reviewed by Hill(84). The stress-strain relationship in torsion have been discussed, among others, by Cottrell(85) and Tegart(86).

Consider the torsion of a round bar. If a cylindrical shell of this bar of length l, radius r and thickness dr, is twisted through an angle θ by the applied force df, as shown below, then the strain is equivalent to a shear OABC - ODEC.

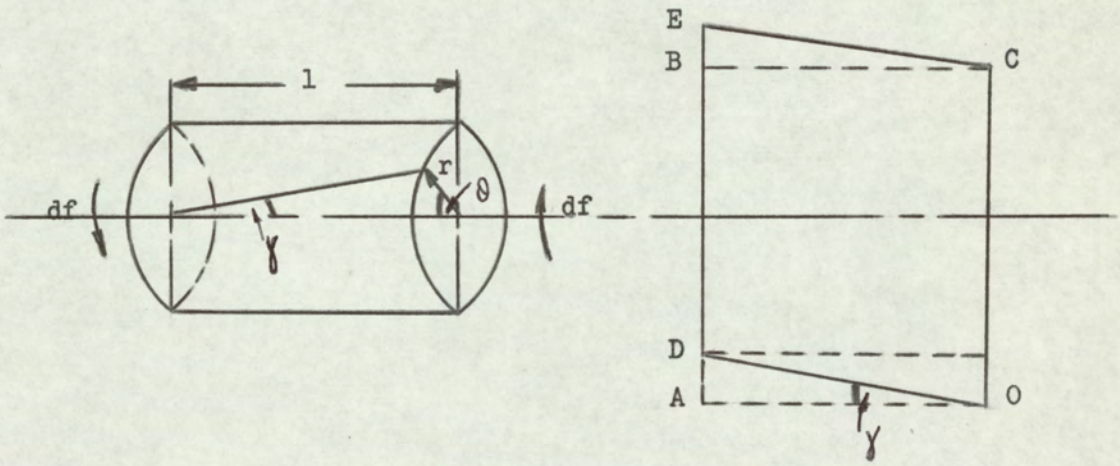

For small strains, where $\tan\theta = \theta$, $AD = l\gamma = r\theta$ and the shear strain is given by;

$$\gamma = \frac{r.\theta}{l} \qquad (3.9)$$

The force, df, acts over an area of $2\pi r.dr$ and the shear stress is;

$$\tau = \frac{df}{2\pi r.dr} = \mu\gamma \qquad (3.10)$$

where μ is the shear modulus.

$$\therefore df = \tau . 2\pi r . dr$$

$$= 2\pi r . dr . \mu \gamma$$

$$= 2\pi r^2 . dr . \mu . \frac{\theta}{l}$$

This force acts tangentially at a distance r from the axis of the cylinder and produces a torque of moment r.df. The total torque, T, on the bar is given by the sum of r.df over all such cylinders upto the outer radius of the cylinder, r_1, as follows;

$$T = \int_0^{r_1} \frac{2\pi r^3 . \mu\theta}{l} . dr$$

and for a thin walled tube the torque is equivalent to;

$$T = \int_{r_2}^{r_1} \frac{2\pi r^3 . \mu\theta}{l} . dr$$

where r_2 is the inner radius of the tube. Thus, in the present work;

$$T = \frac{\pi}{2} . \frac{\mu\theta}{l} . (r_1^4 - r_2^4) \qquad (3.11)$$

By substitution for the shear modulus in this equation the shear stress can be related to the torque as follows;

$$\tau = \left[\frac{2}{\pi (r_1^3 - r_2^3)} \right] T \qquad (3.12)$$

Torsion testing provides a determination of the shear modulus, the limit of proportionality, the yield and maximum stress and strain. In the present research the shear stress at yield and the number of revolutions of the specimen to failure were determined

as a measure of the strength of the material and its ductility respectively. The torsion test results were plotted automatically on a U.V. recorder in terms of the torque and number of revolutions to failure on a time axis as illustrated in Fig.9. The torsion testing machine was calibrated for torque by dead weight loading a beam connected to the axis of the machine. The shear stress at yield was calculated from the torque by equation (3.12) and the number of revolutions to failure by the product of the machine speed and the time to failure of the specimen. The strain rate, $\dot{\gamma}$, is constant for a given gauge length and specimen radius and a given machine speed.

The Torsion Test Specimen

The torsion test specimens were produced by sealing tellurium rod with a stainless steel plug at each end into the cladding tube under an inert argon atmosphere. The 1" long steel plugs were machined to a close tolerance from A.I.S.I. 316L steel to retain the column of liquid tellurium and prevent the collapse of the tube in the grips on torsion testing. A gauge length could not be machined accurately onto the stainless steel tube because the thin walled specimen bowed in the lathe. However, the corrosion provided a gauge length as long as the tellurium rod insert and restricted by the steel plugs. The ends of each specimen were argon-arc welded and the specimens sealed in silica sheaths under vacuum before exposure at temperature.

3.4.2) Scanning Electron Microscopy

The principles, design and uses of the scanning electron microscope have been described by Oatley et al (87) and some of the metallurgical applications discussed by Asbury and Baker(88). A Cambridge Stereoscan was used to examine the fracture of torsion test pieces after testing at room and elevated temperature to determine the nature of, and any change in, the fracture as a result of corrosion by liquid tellurium. The optical microscope is limited in fracture examination by the poor depth of focus and uneven reflection, whereas the scanning electron microscope has a depth of focus some 300 times greater and is mainly limited by the resolution which is ~200°A. This is inferior to that of the transmission electron microscope. However, the Stereoscan was suitable because specimen preparation was negligible and the corroded fractures were unaffected by any mechanical, chemical, or electro-chemical polishing.

4.0) PRELIMINARY RESEARCH RESULTS

The compatibility couples were initially examined by optical microscopy and micro-indentation hardness testing after exposure at temperature for the relevant period of time.

4.1) Optical Microscopy

Compatibility couples containing 0.45grm. of tellurium were exposed at 650°C and 750°C for periods of from 250 hours to 10,000 hours. Couples were examined at intervals of 250 hours upto 1,000 hours and at 2,000 hour intervals from 2,000 hours onwards. Liquid tellurium corroded the A.I.S.I. 316L alloy and resulted in;

i) a transgranular penetration and production of an intermediate phase with a relatively plane advancing interface, and

ii) an intergranular penetration in advance of i).

Tellurium vapour was not adsorbed into the surface of the alloy at vapour pressures of 13.61mms. (650°C) and 60.26mms. (750°C) either in an argon atmosphere, or in vacuo.

The reaction appeared to saturate after ~1,000 hours exposure and in order to study the initial stages of corrosion in more detail a second series of couples were produced containing tellurium rod with exposures limited to this period. The corrosion by liquid tellurium was similar to that in the initial couples, but the higher tellurium content appeared to restrict the intergranular

penetration at 650°C. This was replaced by a 'secondary' trans-granular penetration containing fine precipitated intermediate phase apparently in the grain boundaries of the alloy. The sequence of corrosion by liquid tellurium is illustrated in the two series of optical micrographs at 650°C in Figs.10(a) to 10(f) and Figs. 11(a) to 11(f) at 750°C. The rapid penetration of the liquid phase and the resultant embrittlement of the cladding material is shown in Fig.12 which may be compared with the original couple in Fig.7.

4.2) Micro-Indentation Hardness Testing

The compatibility couples corroded by liquid tellurium were examined by micro-indentation hardness testing along given lines at regular intervals on transverse sections, from the outside of the stainless steel tube to the corroded bore of the alloy. A load of less than 50grms. was necessary to examine the grain boundaries of the alloy where the liquid phase had penetrated. The hardness tests were carried out on both etched and unetched sections at trans- and intergranular positions. One of these hardness traces is illustrated in Fig.13. The error in each hardness was calculated on the basis of the resolving power of the objective ($\pm 0.2\mu$) and squared as in the hardness equation, 3.1). From this figure and many similar ones derived from tests on other couples, there was no definite pattern of hardness variation on tracing from the outside

of the couple to the corroded interface. There was also an overlap in the hardness determined at corroded inter- and transgranular positions for a given load.

The hardness of the iron tellurides which were synthesised for electron probe microanalysis (3.3.3) was determined on mounted sections of each compound. The average hardness of a number of tests with the most suitable load and indenter contact time is given below. The load used in each case was the highest that produced an undistorted indentation.

Phase	V.H.N.	Load (grms.)	Contact Time (secs.)
β	112.0	15	10
γ	337.0	50	10
δ	269.0	50	10
ϵ	419.5	25	10

The γ-phase was segregated to some degree and this segregation was revealed by optical, polarised light microscopy and electron probe microanalysis. The hardness of tellurium was not determined because the lowest load of 15grm. produced a cracked, distorted indentation. The hardness of these synthetic tellurides could not be used to determine accurately the presence of any of these compounds in the corroded alloy because of the overlap in the hardness results from the different sections.

4.3) Conclusions of the Preliminary Results

The conclusions drawn from the results of the preliminary

research were as follows;

i) tellurium vapour at pressures of 13.6mms. and 60.3mms. did not corrode the surface of the A.I.S.I. 316L stainless steel.

ii) liquid tellurium corroded the alloy by transgranular and intergranular penetration.

iii) corrosion by the liquid phase was rapid, eg. a 0.015" wall thickness tube is penetrated in ~1,000 hours at 750°C and resulted in embrittlement of the alloy.

iv) the tellurium content after a 10% burn-up of the fissionable atoms in a fuel pin of the Prototype Fast Reactor may reduce the strength of the cladding material by corrosion at the alloy-fuel interface.

v) the corrosion reaction by liquid tellurium could not be followed by micro-indentation hardness testing.

As a result of this preliminary work, more detailed research was necessary to determine the nature of the corrosion product and the effects of the change in composition of the alloy resulting from the reaction on the mechanical properties of the stainless steel.

5.0) DETAILED RESEARCH RESULTS

5.1) Effect of Corrosion on Alloy Constitution

5.1.1) Penetration by Liquid Tellurium

The trans- and intergranular penetrations of the A.I.S.I. 316L austenitic stainless steel by liquid tellurium at 650°C and 750°C were determined for the couples containing 0.45grms. of tellurium and the tellurium rod. The depths of penetration are plotted as a function of exposure time at constant temperature in Figs.14 and 15. The penetration by liquid tellurium is not a linear function of the exposure time, but reaches a limit at which it remains approximately constant with time. This is particularly evident for the couples containing 0.45grms. of tellurium and the transgranular penetration depths. The effect of this low tellurium content is to restrict the reaction as the tellurium becomes saturated, while the limit on the degree of penetration results from diffusion over greater distances.

5.1.2) X-ray Diffraction

The x-ray diffraction pattern taken from the tellurium is compared with the pattern taken from the A.S.T.M. Card Index (70) (Nos. 4-0554 and 4-0555) in terms of the interplanar spacings in Table 5. The prepared tellurium pattern correlated with the A.S.T.M. Card Index (70) and was used to identify any tellurium lines in the diffraction patterns taken from the product formed by corrosion of the A.I.S.I. 316L steel with liquid tellurium.

The powder pattern of the solution treated austenitic steel consisted of intense F.C.C. lines and extra lines in low contrast. The computed results for the F.C.C. lines are;

$h^2 + k^2 + l^2$	θ°	$\sin\theta^\circ$	$\sin^2\theta$	a(°A)	d(°A)
3	25-41	0.4334	0.1879	3.577	2.065
4	29-59	0.4998	0.2498	3.582	1.791
8	44-56	0.7063	0.4988	3.584	1.267
11	55-47	0.8269	0.6838	3.590	1.082
12	59-46	0.8640	0.7465	3.589	1.036

The lattice parameter of the austenite was determined by extrapolation of the $\sin^2\theta^\circ$ - a(°A) results and found to be 3.595°A. The remaining low intensity lines on the pattern had the following inter-planar spacings

6.020, 4.904, 2.982, 2.686, 2.505, 1.681, 1.605, 1.473, 1.447°A

The sequence of $\sin^2\theta$ values for each line did not fit either a F.C.C., or B.C.C. pattern and could not be analysed with the A.S.T.M. Card Index. The pattern of the stainless steel was used to identify any of the F.C.C. lines present in the powder patterns of the corrosion products.

The synthetic iron tellurides prepared for electron probe microanalysis were examined by x-ray diffraction. The powder patterns corresponded to those given in the A.S.T.M. Card Index (70) except for the γ-phase which was known to be segregated.

A sample of the corrosion product extracted from a couple containing 1.5grms. of tellurium after exposure at 650°C for 1,032 hours had a powder pattern corresponding to the inter-planar spacings

recorded in Table 6. The pattern is similar to that for the binary iron tellurium compound, β-$FeTe_{0.9}$ (A.S.T.M. Card Index No 7-140), except for the presence of three extra lines. These lines are present in the powder pattern for the γ-iron telluride ($FeTe_{1.1}$, A.S.T.M. Card Index No 7-137), but the pattern is a poor fit and the phase is only stable above 750°C. The pattern is similarly a poor fit with that for the δ-iron telluride ($FeTe_{1.5}$, A.S.T.M. Card Index No 7-136), while the 80% intense line at 2.79°A in the ϵ-iron telluride pattern ($FeTe_2$, A.S.T.M. Card Index No 7-367) is absent. No other recorded patterns for the transition metal tellurides fit that of the corrosion product, which appears to be the tetragonal β-iron telluride.

Powder samples extracted from the corrosion product of couples exposed at 650°C and 750°C had patterns similar to the one described above. A sample from the couple corroded by tellurium rod for 1,072 hours at 750°C was chemically analysed and the composition found to be 74.20wt% Te, 16.99wt% Fe, 3.57wt% Cr and 6.04wt% Ni. Although this did not correspond to the expected composition of the β-iron telluride, the analysis did indicate that chromium and nickel were involved in the corrosion reaction. It is difficult to obtain a representative sample in sufficient quantity for chemical analysis and free tellurium may have been present in the analysed sample.

In order to confirm that of the iron tellurides present in

the binary equilibrium diagram the β-phase was the most stable, a couple consisting of pure iron tube (99.90wt% Fe) and tellurium was exposed at 750°C for 168 hours. The diffraction pattern of the corrosion product is recorded in Table 6 in terms of the computed inter-planar spacings. The pattern corresponds to that for the β-iron telluride and the composition determined by electron probe microanalysis was 68.3wt% Te, 32.2wt% Fe. This is similar to the composition for the β-phase and confirms the stability of this compound in a binary iron-tellurium couple under the present conditions.

5.1.3) Electron Microscopy

Two-stage carbon replicas shadowed with gold-palladium alloy were taken from transverse sections of couples corroded by liquid tellurium and lightly etched electrolytically in 10wt% oxalic acid. The replicas showed two distinct phases; a globular precipitate associated with the grain boundaries of the stainless steel and a rod-shaped precipitate presumably the corrosion product, which was less than 1μ long. These two precipitates in a couple exposed at 650°C for 240 hours are illustrated in the electron micrographs in Fig.16. The grain boundary precipitate is probably a carbide of the type $M_{23}C_6$, because the solution treatment temperature for this alloy is below that for complete solution of the carbide given by Blenkinsop and Nutting(40). The size of the precipitate in the corroded region is such that the results of electron probe microanalysis are average

compositions of the area examined.

Extraction replicas were taken from sections of the couples which had not been corroded in order to determine the precipitates present in the stainless steel. After ~1,000 hours exposure at both 650°C and 750°C a rod-shaped precipitate was detected at the grain boundaries of the steel and within the austenite grains as shown in Fig.17. This precipitate was identified by selected area diffraction as the carbide, $M_{23}C_6$, as illustrated in Fig.18.

A similar precipitate was detected by Barnby and Smith(89) in an A.I.S.I. 316 austenitic stainless steel after ageing at 800°C for 500 hours. The precipitation that occurs in this alloy has been described in the literature (40,43,89,90) and the intention was not to repeat this, but to examine the corroded couples knowing that precipitation will occur in the stainless steels under the present compatibility conditions. The rod-shaped carbide can interfere with the recognition of the precipitate in the corroded regions of low precipitate density and in dense precipitate areas, identification by a single crystal pattern is difficult because of precipitate clustering.

The precipitate extracted from the corroded areas of the couples is illustrated in Fig.19. The replicas were taken from a couple exposed at 650°C for ~1,000 hours and the precipitate was identified as the β-iron telluride by selected area diffraction.

5.1.4) Electron Probe Microanalysis

Preliminary Analysis

Corrosion by the liquid phase produced a change in the constitution of the alloy at the surface in the region of transgranular penetration and in the grain boundary area as a result of the intergranular penetration. The effect of the diffusion by liquid tellurium is illustrated quantitatively in Fig.20. The tellurium concentration in the region of transgranular corrosion is not a linear function of the distance from the original interface and the solubility in the austenite outside of this area is very small. The composition at point 1 had a tellurium content similar to the β-iron telluride, but the compound was not the 'simple' binary because small amounts of chromium and nickel were present corresponding to a compound of the type MeTe where Me is the sum of the iron, nickel and chromium contents.

The result of intergranular penetration on the composition of the grain boundary regions is illustrated in Fig.21. The penetration is associated with the tellurium peaks and the corresponding iron, nickel and chromium troughs. Molybdenum appears inactive in the reaction. The tellurium contents in the grain boundaries were too low to form any known telluride.

Detailed Analysis

The corrosion reaction was studied systematically by analysis

of diffusion couples containing tellurium rod and exposed at 650°C and 750°C for periods of upto 1,000 hours. The results are presented as a pertinent series of trace analyses with corresponding x-ray and electron micrographs.

After 1 hour exposure there was an abrupt change in the constitution of the steel at the limit of transgranular penetration and the composition of the interface corresponded to a telluride of the type MeTe, where Me is the sum of the iron, nickel, manganese and chromium contents, but rich in the latter. This is 'similar' to the hexagonal chromium telluride CrTe. The diffusion of tellurium into the alloy was accompanied by the transport of the elements of the alloy in the opposite direction towards the original tellurium. The composition at the reaction interface after 4 hours exposure corresponded to MeTe, but the iron and chromium contents were present in similar amounts.

The interfacial regions became more complex after 16 hours exposure, as illustrated in Fig.22 with the composition of the interface corresponding to MeTe. However, compounds with tellurium contents rich in iron similar to the β-iron telluride and chromium-rich, similar to the hexagonal chromium telluride were both determined.

After a prolonged exposure for 239.5 hours at 750°C intergranular penetration was evident even at the low magnification required to analyse a complete section. This is illustrated in the

analysis Fig.23 and the electron and x-ray micrographs in Fig.24. The point analysis indicate three possible compounds, one of the type $MeTe_{1.5}$ and two similar to MeTe. The first two are rich in chromium and the third rich in iron, but none were equivalent to the binaries. Chromium appears to be at least as active in the reaction as iron.

Each of the three regions illustrated in Fig.23 namely the trans- and intergranular penetrations and the remnant tellurium were examined in detail at high magnification. The intergranular penetration of tellurium is shown in Fig.25 and the resultant analysis along the line shown is as follows;

Position	Te	Fe	Ni	Cr (wt%)
Transgranular point	0.70	65.82	11.42	17.14
Intergranular point	11.24	78.26	2.22	3.29
Transgranular point	0.89	65.16	10.12	18.53
Intergranular point	59.59	26.35	6.28	17.40

Te-rich area

In the region of transgranular penetration the iron is concentrated in areas which are relatively low in tellurium as shown in the following analysis;

Position	Te	Fe	Ni	Cr (wt%)
Te-rich matrix	79.17	5.36	0.24	15.77
Fe-rich area	66.59	15.39	0.58	15.87
Fe-rich area	56.47	28.26	0.90	11.08
Fe-rich area	47.77	40.61	0.97	11.19

Original stainless steel

Only one of the iron-rich areas contains sufficient tellurium to form

a known telluride and that is the area with 66.59wt% Te. The compound is of the type MeTe and contains both iron and chromium producing a ternary phase. On the side of the couple which had originally contained tellurium the composition corresponded to 82.98wt% Te, 5.32wt% Fe, 0.78wt% Ni and 18.75wt% Cr.

Complete grain boundary penetration of the couple occurred after 1,072.5 hours exposure at 750°C and the analysis of the couple is presented in Fig.26. On the tellurium-rich side of the couple the analysis corresponded closely to the hexagonal chromium telluride CrTe, but small amounts of iron, nickel and manganese were present as in the following analysis; 69.12wt% Te, 5.76wt% Fe, 0.05wt% Ni, 21.76 wt% Cr, 1.24wt% Mn and 1.77wt% Mo. This compound was recognised in the area of transgranular corrosion along with one corresponding to MeTe containing both iron and chromium. In this region areas rich in iron were detected with the iron content ranging from 64.41 to 82.81 wt%. This is illustrated in Fig.27 and the analysis of two of these areas is given below;

Position	Te	Fe	Ni	Cr (wt%)
Te-rich matrix	75.06	9.72	0.83	16.78
Fe-rich area	17.82	66.43	4.25	8.23

The penetration which results after 1,072.5 hours at 650°C is illustrated in Fig.28. The analyses corresponds to compounds of the form $MeTe_{1.5}$, rich in chromium and MeTe, rich in both chromium and iron.

5.2) Effect of Corrosion on Mechanical Properties

5.2.1) Torsion Testing

A series of compatibility couples were produced for torsion testing at room and elevated temperature. Before and after exposure, each couple was weighed on a chemical balance to determine any change in weight as a result of oxidation, or leakage. The results are recorded in Table 7 and show a negligible weight change, considering an error of ± 0.0007grms. on the balance over 34 readings.

After exposure each specimen was machined to a length of 3.5ins. eg. the crimped and welded ends of the couple were removed, for positioning in the grips and tested at either room temperature, or 600°C, at a constant strain rate of $0.11 sec^{-1}$.

The shear stress at yield is plotted as a function of time at constant temperature for each series of test specimens in Fig.29. The reduction of the shear stress for the control test specimens, which reaches a limit at approximately 100 hours, is probably a result of stress relief on ageing at temperature of the cold worked alloy. The shear stress is reduced more rapidly and to a greater extent for the corroded couples. The reduction is greater after exposure at the higher temperature and for torsion testing at 600°C, and is not a linear function of the exposure time.

The effect of corrosion by liquid tellurium on the ductility of the stainless steel is illustrated in Fig.30 for each series of

torsion test specimens. The control specimens show some increase in ductility upto a limit at approximately 100 hours exposure which corresponds to the stress relief illustrated by the shear stress at yield upon ageing the alloy. The ductility of the alloy is reduced by corrosion, the reduction being greater after exposure at the higher temperature. Torsion testing at 600°C showed some increase in the ductility over the specimens tested at room temperature and this may have been a result of greater plasticity at the higher temperature.

5.2.2) Fracture Studies

The fracture of the torsion test specimens was basically one of shear, exhibited by the control specimens and the corroded couples exposed for the shorter times, tested at both room and elevated temperature. This type of fracture is illustrated in Fig.31.

However, the specimens corroded for the longest times and tested at both room temperature and 600°C showed a fracture with some degree of tearing, illustrated in Fig.32. The examination of the fracture faces was limited by the depth of focus of the optical microscope, but this was overcome by the use of a scanning electron microscope.

The control specimens which were torsion tested at room temperature and 600°C had ductile, transgranular fractures characterised by the 'dimpled' appearance illustrated in Fig.33. The corroded couples exposed at 650°C and at 750°C for the shorter times had a

similar 'dimpling' in the remaining stainless steel, but the corroded area illustrated brittle fractures as in Fig.34. The tellurium which remained in the bore of the couple appeared to cleave during the torsion test as shown in Fig.35. This figure also illustrates the brittleness produced during corrosion by fracture at the interface between the corroded layer and the stainless steel. The compatibility couples exposed for the longest times at temperature exhibited both the fracture which occurred in the corroded areas and propagated towards the stainless steel Fig.36 and the fracture occurring in the region of intergranular penetration, Fig.37.

6.0) DISCUSSION

The compatibility study has shown that A.I.S.I. 316L austenitic stainless steel is corroded by liquid tellurium and that the extent of reaction depends initially upon the tellurium content of the compatibility couple. This confirms the observations made by Wells(67) in a limited study with an austenitic stainless steel of a different composition, namely a 20Cr-25Ni-Nb alloy and the limitation on the extent of reaction appears to be a result of the saturation of the liquid phase as reaction continues. The corrosion exhibited by tellurium cannot be categorised simply as one of the various known types of liquid metal corrosion discussed in the literature survey (2.2). This is because of both the fundamental difference in chemistry between the reactants and the complex composition of the austenite. Thus tellurium has a limited solubility in the F.C.C. lattice as shown by electron probe microanalysis (5.1.4) and forms intermetallic compounds with the transition metals that constitute the austenite. Consequently, an intermediate phase is formed during corrosion and both trans- and intergranular penetration of the liquid phase takes place. The degree and rate of reaction depend upon the diffusion of tellurium through the corroded area and along the alloy grain boundaries, provided sufficient liquid is present in the system to stimulate reaction. This diffusion of tellurium into the alloy is accompanied by both a swelling of the cladding material, as shown in Fig.12 and the transport of the con-

stituents of the alloy into the tellurium-rich side of the couple in order to accommodate the diffusion. Therefore the present reaction overlaps into three of the types of liquid metal corrosion indicated previously, namely types ii), iv) and v).

The corrosion affects both the mechanical properties and constitution of the stainless steel and the latter indicates the possible reaction mechanism.

6.1) The Effect of Corrosion on Mechanical Properties

The reduction in the shear stress at yield for the torsion test specimens exposed at the two different temperatures and tested at both 25°C and 600°C corresponds with the degree of corrosion exhibited by each series of specimens. The results can be analysed on a logarithmic basis in terms of the reduction in shear stress at yield, not the absolute value, as a function of the exposure time according to the following equation;

$$y = a.x^n \qquad (6.1)$$

where y is the reduction in yield shear stress, x the exposure time and a and n constants. By taking logarithms this equation becomes;

$$\log_{10} y = \log_{10} a + n \log_{10} x \qquad (6.2)$$

which is a linear plot of slope n. The reduction of the shear stress at yield is plotted on this basis as a function of the exposure time in Fig.38. This figure illustrates clearly how the increased penetration at 750°C (curve a) compared with 650°C (curve b) reduces the

shear stress. The results of testing at 600°C are plotted as curve(c) which lies between the former two. However, if these results are calculated using the room temperature shear stress for the control specimens as with curves(a) and (b), curve(d) is obtained. This now lies in the correct sequence and illustrates the adverse affect of corrosion on the high temperature strength of the alloy. If the values of the two constants in equation (6.1) are known then the shear stress at yield, after corrosion for a given time at temperature under the present conditions can be calculated. The values of these constants are tabulated below;

Compatibility Conditions	Constants	
	a	n
650°C corrosion, test at 25°C	1.24	0.16
750°C corrosion, test at 25°C	2.27	0.18
750°C corrosion, test at 600°C	1.47	0.15

The ductility of the torsion test specimens is also a linear function of the exposure time at constant temperature when plotted on a logarithmic scale as shown in Fig.39 and obeys a law similar to that given by equations (6.1) and (6.2), where y is now the ductility. The values of the constants a and n allow the ductility of the corroded couples to be determined after a given exposure at constant temperature and are tabulated below;

Compatibility Conditions	Constants	
	a	n
650°C corrosion, test at 25°C	0.65	-0.09

750°C corrosion, test at 25°C	0.62	-0.28
750°C corrosion, test at 600°C	1.13	-0.39

The effect of corrosion by liquid tellurium on the mechanical properties of the austenitic stainless steel reduces the shear strength at yield and the total ductility to failure of the alloy. The degradation observed is greatest for corrosion at the longer exposure times and the higher temperature, which is a direct result of the increased degree of corrosion. Both the room and elevated temperature properties of the alloy are affected in a similar way.

Corrosion by liquid tellurium altered the fracture of the austenitic alloy, depending upon the degree of corrosion. The control torsion test specimens exhibited a ductile, transgranular fracture, while the corroded specimens fractured in a brittle manner in the corroded area. This followed an intergranular path in the couples exhibiting grain boundary penetration. The remaining tellurium appeared to cleave and crack initiation probably occurred here and propagated through the corroded area towards the outer surface of the stainless steel resulting in ultimate failure of the couple. The tearing illustrated in Fig.32 was thought to be due to the lack of cohesion between the corroded area and the remaining alloy as a result of the increased embrittlement after prolonged exposure in both room and elevated temperature tests.

6.2) The Effect of Corrosion on Alloy Constitution

The transgranular penetration by liquid tellurium resulted in production of an intermediate phase at the surface of the alloy. This phase was shown by x-ray diffraction to have a structure similar to that of the β-iron telluride ($FeTe_{0.9}$) and no other phase could be determined by this technique. The telluride existed in the form of rod-shaped particles less than 1μ in length as illustrated in Fig.16 and as such only allowed an average composition to be determined by electron probe microanalysis.

The iron telluride was not expected to form because the manganese telluride (MnTe) is apparently thermodynamically more stable as shown in Fig.6. Both the nickel ($NiTe_{1.1}$) and manganese ($MnTe_2$) tellurides appear more stable than the β-$FeTe_{0.9}$ compound, but the calculation of the free energies of formation for both of these contained estimated property values (2.2.2) and consequently may be in error. The iron ($FeTe_{0.9}$) and manganese (MnTe) tellurides were both shown to be stable under the present compatibility conditions. Thus, the β- phase was formed from a couple consisting of pure iron and tellurium exposed at 750°C (5.1.2), while manganese and tellurium diffused together for 379 hours at 750°C resulted in a single hexagonal structure corresponding to that given by Greenwald for the MnTe compound (91). Consequently, both compounds will form from the elements in their standard states under the present conditions and

confirm the calculated thermodynamic data. Preferential compound formation also reduces the degree of corrosion by tellurium. However, both the iron and manganese are present in solution in austenite and not in their standard states, with the iron in the largest proportion acting as the alloy base. Although Raoult's law was assumed this is not strictly applicable because of the large amount of alloy present in the lattice. Therefore, although chemical thermodynamics indicated the stability of the transition metal tellurides the order of stability with the elements in solid solution appears to be in error. However, this may be due to the reaction kinetics.

A compound of the type ε-$FeTe_2$ was said to form and be the most stable in reaction between a 20Cr-25Ni-Nb alloy and liquid tellurium by Wells(67). However, even considering the difference in alloy composition the present theoretical and experimental work indicates that the β-iron telluride would most probably form. Horseley(68) in a titanium-stabilised 18Cr-8Ni alloy found that tellurium vapour at pressures of 0.002mms. and 0.6mms. corroded the alloy surface with consequent production of the $MeTe_{1.4}$ compound (2.2.1). However, at pressures of 13.6mms. and 60.3mms. the vapour was not found to corrode the present alloy, either under a vacuum, or an atmosphere of argon. There is no apparent reason for this lack of reaction, unless initial wetting of the surface as illustrated by the liquid phase is required for corrosion.

The transgranular penetration by tellurium resulted in an intermediate phase and the low solubility shown can be illustrated in the following way. The lattice parameter of the austenite is equivalent to an 'atomic diameter' of $a\frac{\sqrt{2}}{2}$, or 2.542°A, while the largest interstice is the B.C.C. position equal to 0.41r, or 0.5211°A where r is the 'atomic radius'. The 'diameter' of the tellurium atom is 2.87°A, too large to be accommodated interstitially, but just within the 15% limit suggested by Hume-Rothery for substitutional solid solution. This low solubility will limit the diffusion of tellurium in austenite and the transport of the element will then depend on diffusion through the corroded areas.

A single, binary compound of the β-$FeTe_{0.9}$ type could not be determined by electron probe microanalysis, but compositions which corresponded to possible ternary and higher tellurides were analysed in the band of transgranular penetration. The intergranular penetration did not consist simply of the pure element since the tellurium contents of the grain boundary regions were relatively small and decreased away from the original tellurium-steel interface. After 4 hours exposure a compound similar to MeTe, where Me is equal to the sum of the iron, nickel, chromium, manganese and molybdenum contents and rich in chromium was analysed in the region of transgranular penetration, but with increasing exposures the compound became rich in both iron and chromium. As the corrosion pro-

gressed, compositions corresponding to more than one telluride were found. For example, after 16 hours exposure at 750°C both iron- and chromium-rich compounds of the type MeTe were analysed, while other compounds detected upon prolonged exposure included one, rich in chromium, of the form $MeTe_{1.5}$. However, the importance of electron probe microanalysis did not lie solely in phase identification, but more in following the change in composition across the reaction interface as corrosion occurred in order to deduce the mechanism of the exchange.

The limit of transgranular penetration is always clear by the abrupt change in alloy composition as illustrated in Fig.20. The tellurium content decreases in an irregular manner across the corrosion zone and coincides with a similar decrease in iron content of the alloy in the opposite direction. The alloy nickel and chromium contents decrease abruptly at the limit of penetration and then change irregularly across the corroded area, especially with increasing exposures, while the change in the manganese content of the alloy is more gradual. The transport of the nickel, chromium and manganese atoms probably occurs by a 'leaching' process, while the iron forms the β-telluride in situ. An extensive 'leaching' process, however, is not expected because of the low solubilities involved, but there is some evidence of a transport mechanism since the elements of the stainless steel were detected by electron probe microanalysis

on the tellurium-rich side of the couple. It may be that in the presence of the iron other tellurides are unstable, but this is only a tentative suggestion and there is no direct evidence.

6.2.1) The Activation Energy of Reaction

In order to equate the time, temperature and depth of penetration, a rate of penetration is required at each temperature. The penetration rate after each exposure at constant temperature is recorded in Table 8 and is seen to decrease with increasing time of exposure from some maximum value at the onset of corrosion. A representative value of the rate at the start of corrosion is necessary in order to determine the energy of activation for the penetration. The rate of penetration cannot be calculated from the slope of the penetration-exposure time curves in Figs. 14 and 15, but the average value, or the rate at some given exposure could be calculated. However, the logarithm of the rate of penetration is a linear function of the exposure time, illustrated in Fig.40 and obeys a law of the form;

$$y = a.x^n \qquad (6.3)$$

where y is the penetration rate, x the exposure time and a and n constants. The value of the constant, a, provides a rate which can be used to determine the activation energy for the penetration.

The activation energy can be calculated from the rate of penetration by an equation of the form;

$$\text{Rate} = A.\exp(-Q/RT) \qquad (6.4)$$

where A is a constant, Q the energy of activation, R the gas constant and T the absolute temperature. By taking logarithms equation (6.4) becomes;

$$\text{In.(rate)} = \text{In.A} - Q/RT \qquad (6.5)$$

$$\text{or } \log_{10}\text{rate} = \log_{10}A - \frac{Q}{2.303R}\cdot\frac{1}{T} \qquad (6.6)$$

Consequently, the logarithmic rate should be a linear function of the reciprocal of the absolute temperature with a slope $(-Q/2.303R)$, which can be used to calculate the activation energy. In the present work only two temperatures, 650°C and 750°C, were used at the different tellurium levels and the energies of activation were determined directly from the penetration rates rather than from the slope of the curve. The values of the rates and energies of activation at the two levels of tellurium content are as follows;

i) 0.45grms. of Te

Temperature(°K)	Rate of Penetration(μ.hour^{-1}) Intergranular	Transgranular
923	23.33	29.20
1,023	84.53	48.93
Activation Energy (K.cals.mole^{-1})	25.0 ±5.0	10.0 ±2.0

ii) Te rod

Temperature(°K)	Rate of Penetration(μ.hour^{-1}) Intergranular	Transgranular
923	38.11	18.85
1,023	60.24	38.35

Activation Energy (K.cals.mole-1)	9.0 ±2.0	14.0 ±3.0

The error in the activation energies was calculated from the errors involved in determining the depths of penetration. These were measured to ±2.5μ, while the inaccuracy in sectioning was 5° maximum, equivalent to a linear measure of ±1.8μ on any section. Thus, the total error was ±4.3μ, or a maximum of 20% in the calculated energy values.

Within the limits of accuracy the energy of activation for transgranular penetration is similar at the two different levels of tellurium content, but there is a discrepancy between the energies calculated for intergranular penetration. Now, because the transgranular penetration appears to occur initially followed by the grain boundary corrosion a higher energy would be expected for the latter process. However, because of the disorder of the grain boundary regions intergranular penetration should theoretically require a lower energy since accommodation is relatively easier. It cannot simply be assumed that the grain boundary penetration requires a higher activation energy, because of the greater rate of penetration since the energy is calculated on a rate difference and not the absolute rate. With a low tellurium content the threshold time for a grain boundary reaction could be higher because of the difference in available area presented by the grain and grain boundary regions,

resulting in an apparently higher activation energy. Consequently, an error may arise in the determination of energy values when a small quantity of one of the reactants is involved because of the physical nature of the system. Therefore, the activation energies calculated for the couples containing the high tellurium content were deemed the most accurate. The value of the energies for both types of penetration are now of a similar order and this explains why a grain boundary penetration does not take place prior to a bulk, or transgranular corrosion in the early stages of reaction. As the reaction progresses the concentration gradient decreases and a transgranular movement becomes more difficult over the longer distances involved. Grain boundary penetration then becomes energetically more favourable. The values of activation energy are low by comparison with other systems. Cheney et al (92) for example, determined a value of 20K.cals.grm.atom^{-1} for the penetration of bismuth in copper and the present low value is probably because of the chemical affinity shown between the reactants in the present study.

6.2.2) <u>The Role of Diffusion</u>

The process of diffusion has been discussed in detail in the literature, among others by (93-96). The formal theory of diffusion is based upon Fick's laws which are basically ideal, limiting laws and work has been carried out on the solutions of these for various boundary conditions assuming a constant diffusion coefficient.

For steady-state diffusion Fick's first law is given by the following;

$$J = -D\frac{\partial c}{\partial x} \qquad (6.7)$$

where J is the flux, D the diffusion coefficient and $\partial c/\partial x$ the concentration gradient. In the present research the equation would consist of a number of coefficients because the diffusion couple is essentially a multi-component system. Therefore, the solution of the first law would be of the following form;

$$J_1 = -D_{11}\frac{\partial c_1}{\partial x} - D_{12}\frac{\partial c_2}{\partial x} - D_{13}\frac{\partial c_3}{\partial x} - D_{14}\frac{\partial c_4}{\partial x} - D_{15}\frac{\partial c_5}{\partial x} - D_{16}\frac{\partial c_6}{\partial x}$$

$$J_2 = -D_{21}\frac{\partial c_1}{\partial x} - D_{22}\frac{\partial c_2}{\partial x} \text{ --- etc.}$$

down to

$$J_6 = -D_{61}\frac{\partial c_1}{\partial x} - D_{62}\frac{\partial c_2}{\partial x} \text{ --- etc.}$$

in order to account for the transport of tellurium and each of the major constituents of the stainless steel. In order to simplify the solution and account for the non-steady state conditions, the system was treated as a pseudo-binary and analysed according to Fick's second law, which is given as follows;

$$\frac{\partial c}{\partial t} = \frac{\partial}{\partial x}\left(D\frac{\partial c}{\partial x}\right) \qquad (6.8)$$

where $\partial c/\partial t$ is the rate of change of concentration. If the diffusion coefficient is considered constant at constant temperature equation (6.8) becomes;

$$\frac{\partial c}{\partial t} = D\frac{\partial^2 c}{\partial x^2} \qquad (6.9)$$

The solution of this differential for a semi-infinite system is given by the following;

$$\frac{Cx - Co}{Cs - Co} = 1 - \varphi\left(\frac{x}{2\sqrt{Dt}}\right) \qquad (6.10)$$

where Cx is the concentration of the diffusing element at some distance x, after a time t, Co the initial uniform concentration and Cs the constant surface concentration. The function $\varphi(y)$ is the Gaussian Error Function. This simplification is believed justified because the corrosion involves formation of an iron telluride and the solubilities of the remaining reactants are limited. Consequently the austenite-tellurium couple is reduced to the $FeTe_{0.9}$ -Te system.

Since both trans- and intergranular penetration by liquid tellurium occurred, coefficients for volume and grain boundary diffusion were determined. The volume diffusion coefficient was determined at distances perpendicular to the reaction interface, but the grain boundary diffusion coefficient was more difficult to calculate. This was achieved, however, by considering the diffusion distance as the sum of both the trans- and intergranular penetrations and calculating the coefficient on the basis of the average grain size of the alloy. The coefficients determined in this way for each couple did vary. For volume diffusion at 750°C the coefficient lay between

1.4 and 3.4 x 10^{-11} $cms.^2 sec.^{-1}$, while for grain boundary diffusion the values were between 2.0 and 5.5 x 10^{-11} $cms.^2 sec.^{-1}$. The values for the two coefficients were both small and similar. The grain boundary diffusion coefficient was expected to be some orders of magnitude higher than that for volume diffusion, while the small values indicated the limited diffusion in the system. The variation in the coefficients was probably because of both the simplification of the system and the complex changes that occurred in the composition of the couple. For these reasons it was therefore thought more significant to describe the process empirically on the basis of the change in composition that occurred as reaction took place.

6.3) The Mechanism of Corrosion

The mechanism of the corrosion of the austenitic stainless steel by liquid tellurium can be examined in terms of both the activation energy for penetration by the liquid phase and the resultant embrittlement of the alloy, while a model which explains the observed results can be described on the basis of the change in composition of the compatibility couple as corrosion proceeds.

The activation energy for penetration by liquid tellurium is similar to the free energy of formation of the β-iron telluride, as illustrated below.

Free Energy of Formation ($K.cals.mole^{-1}$)	650°C	750°C
Iron in its standard state	13.0	11.0

Iron in solution in austenite	12.0	10.0

Activation Energy(K.cals.mole^{-1})

Transgranular penetration	14.0 ±3.0
Intergranular penetration	9.0 ±2.0

The free energy for the formation of the telluride with iron in solution in the austenite was calculated assuming Raoultion conditions, although this is not strictly applicable as discussed previously. This similarity in values indicates that the initial stage of reaction at least is controlled by the formation of the telluride, whether or not this is modified by tellurium diffusion at a later stage.

Since the initial stage of the reaction appears to be controlled by liquid tellurium penetration it may be assumed that the degradation in mechanical properties of the alloy is dependent upon the extent of penetration. However, the embrittlement which occurs is not simply proportional to the depth of penetration by the liquid phase. This is illustrated by comparing the degree of penetration with the reduction in both the shear stress at yield and the total ductility (the number of revolutions to failure of the specimen) of the alloy calculated as a percentage of the original values for the uncorroded steel as given in Table 9. From these values it appears that the percentage embrittlement of the alloy is greater than the degree of penetration by liquid tellurium. This is more obvious at the higher temperature and for the calculated ductility. Con-

sequently, although the reaction depends initially on the formation of the telluride the embrittlement of the alloy is not solely dependent on the propagation of this compound.

The corrosion occurs by the diffusion of tellurium into the austenite lattice with the consequent change in the alloy constitution as a result of formation of a telluride(s). The diffusion is accommodated by an apparent increase in volume of the austenite lattice which may ultimately lead to failure as illustrated in Fig. 12, and by transport of the alloy constituents towards the tellurium-rich side of the compatibility couple. The reaction occurs by both trans- and intergranular penetration, but since the activation energies for penetration are similar, only the former is apparent in the early stages of corrosion. Upon prolonged exposure incomplete reaction may lead to remnant crystals within the area of transgranular penetration. These crystals are rich in iron and devoid of the other alloy constituents.

The chemical affinity of tellurium for the transition metals limits the transport of tellurium in austenite and reaction continues by diffusion of this element through the corroded region. This chemical affinity between the reactants prevents any 'self-inhibition' of the reaction. The diffusion of tellurium controls the penetration as reaction proceeds and this accounts for both the initial high rate of penetration and the decrease in rate with time

at both temperatures as transport is necessary over longer distances. With increased exposure as the concentration gradient across the couple is decreased, diffusion of tellurium in the alloy grain boundaries is energetically more favourable resulting in the visible intergranular penetration.

Thus, the corrosion occurs by penetration of the liquid tellurium which is initially controlled by the formation of a telluride and ultimately by diffusion of tellurium through the corroded region as reaction continues.

7.0) CONCLUSIONS

The conclusions drawn from this compatibility study between A.I.S.I. 316L austenitic stainless steel and tellurium are as follows;

i) liquid tellurium corrodes the alloy, but the rate of corrosion decreases with increasing time of exposure at constant temperature.

ii) the resultant change in alloy composition leads to the formation of a telluride and

iii) degrades the alloy by inducing embrittlement.

iv) corrosion will possibly be retarded by preferential formation of a telluride, thus precluding tellurium from wetting the alloy surface.

8.0) FUTURE WORK

This compatibility study illustrated what little data on phase equilibria in the binary tellurium-transition metal systems is available in the literature and the difficulty in studying diffusion in a multicomponent system. Therefore, future work could be composed of a determination of the phase relationships in the binary systems and a study of diffusion in the binary couples. It may also be possible to alter the alloy constitution in order to preferentially form a telluride other than iron and so restrict the reaction and reduce the degree of embrittlement.

9.0) ACKNOWLEDGMENTS

The author wishes to thank the U.K.A.E.A. for financial support and Professor W. O. Alexander for provision of laboratory facilities. The author also wishes to acknowledge the useful discussion with Dr. J. A. Wright.

10) REFERENCES.

1) Stephenson, R. Introduction to Nuclear Engineering, McGraw-Hill, 1954.

2) Engineering, 1962, 194, 561.

3) Herbert, D. New Scientist, 1962, 14, 336.

4) Philips, J. L. Nuclear Engineering, 1965, 10, 264.

5) Engineering and Boiler Review, 1962, 77, 430.

6) Engineer, 1966, 221, 267.

7) Nuclear Engineering, 1966, 11, 182.

8) Frame, A. G. and Mathews, R. R. Nucleonics, 1966, 24, 54.

9) Fawcett, S. Atom, 1965, 108, 208.

10) Eickhoff, K. G. Atom, 1966, 115, 98.

11) Frame, A. G. et al. Atom, 1966, 116, 134.

12) Evans, P. Fast Breeder Reactors, Pergamon, 1967.

13) Medin, A. L. Metal Progress, 1963, 83, 109.

14) Chiswik, H. H. J. Metals, 1960, 12, 236.

15) Wright, J. C. Metal Treatment and Drop Forging, 1961, 28, 21.

16) Nuclear Engineering, 1966, 11, 528.

17) Lawton, H. Atom, 1966, 111, 11.

18) McIntosh, A. B. and Bagley, K. Q. J. Brit, Nucl. Energy Soc. Conf. 1958, 3, 15.

19) Bagley, K. Q. Nuclear Engineering, 1957, 2, 461.

20) McIntosh, A. B. and Grainger, L. J. J. Brit. Nucl. Energy Soc. 1962, 1, 3.

21) Howe, J. P. Progress In Nuclear Energy, Series V, Metallurgy and Fuels, Pergamon, 1956, 1, 1948.

22) Hansen, M. Constitution Of Binary Alloys, McGraw-Hill, 1958.

23) Elliot, R.P. Constitution Of Binary Alloys, First Supplement, McGraw-Hill, 1965.

24) Colombier, L. and Hochman, J. Stainless and Heat Resisting Steels, Arnold, 1965.

25) Schafmeister, P. and Ergang, R. Arch. Eisenh. 1938-39, 12, 459.

26) Kinzel, A. B. and Franks, R. The Alloys Of Iron and Chromium, McGraw-Hill, 1942, 2.

27) Cook, A. J. and Brown, B.R. J.I.S.I. 1952, 171, 345.

28) Rees, W. P. et al. J.I.S.I. 1949, 162, 325.

29) Hattersley, B. and Hume-Rothery, W. J.I.S.I. 1966, 204, 683.

30) Price, P. E. and Grant, W.J. Trans. A.I.M.E. 1959, 215, 635.

31) Franks, R. Binder, W. O. and Bishop, C. R. Trans. A.S.M. 1941, 29, 35.

32) Pops, H. J.I.S.I. 1966, 204, 1117.

33) Schaeffler, A.L. Metal Progress, 1949, 56, 680.

34) Delong, W. T. Metal Progress, 1960, 77, 98.

35) Cope, L. H. TRG Report 283(D), 1962.

36) Thielsch, A. Welding J. Research Supplement, 1950, 29, 577s.

37) Oliver, D. A. Metal Progress, 1949, 55, 665.

38) Talbot, A. M. and Furman, D. E. Trans. A.S.M. 1953, 45, 429.

39) Lena, A.J. and Curry, W. E. Trans. A.S.M. 1955, 47, 193.

40) Blenkinsop, P. A. and Nutting, J. J.I.S.I. 1967, 205, 953.

41) Hall, E. O. and Algie, S. H. Met. Rev. 1966, 11, 61.

42) Mahla, E. M. and Neilsen, A. Trans. A.S.M. 1951, 43, 290.

43) Lewis, M. H. and Hattersley, B. Acta Met. 1965, 13, 1159.

44) Mazza, J. A. J.I.S.I. 1966, 204, 783.

45) Barnby, J. T. J.I.S.I. 1966, 204, 23.

46) Mazza, J. A. and Willoughby, G. J.I.S.I. 1966, 204, 718.

47) Hopkins, L. M. T. and Taylor, L. H. J.I.S.I. 1967, 205, 17.

48) Cottrell, A. H. Brit. Nucl. Energy Soc. Conf. 1958, 3, 50.

49) Blackburn, R. Met. Rev. 1966, 11, 159.

50) Bement, A. A.S.T.M. Sp. Tech. Publ. 418, A.S.T.M. 1967.

51) Roy, R. B. and Sully, B. J.I.S.I. 1967, 205, 58.

52) Waddington, J. S. Met. Sci. J. 1967, 1, 156.

53) Higgins, P. R. B. and Roberts, A. C. J.I.S.I. 1966, 204, 409.

54) Broomfield, G. H. Harries, D. H. and Roberts, A. C. J.I.S.I. 1965, 203, 502.

55) Eldred, V. W. A.E.R.E. X/R. 1806. Harwell, 1956.

56) Rostoker, W. McCaughey, J. M. and Markus, H. Embrittlement By Liquid Metals, Reinhold, 1960.

57) Elbaum, C. Trans. Met. Soc. A.I.M.E. 1959, 215, 476.

58) Cheney, R. et al. Trans. Met. Soc. A.I.M.E. 1961, 221, 492.

59) Thomson, R. J.I.M. 1968, 96, 28.

60) Manly, W. D. Corrosion, 1956, 12, 46.

61) Brasunas, A. deS. Corrosion, 1953, 9, 78.

62) Miller, E. C. Liquid Metals Handbook, U.S.A.E.C. 1952, 144.

63) Weeks, J. R. and Klamut, C. J. Corrosion Of Reactor Materials Int. Atomic Energy Conf. Vienna, 1962, 1, 105.

64) Frost, B. R. T. J. Nuclear Mats. 1962, 7, 109.

65) Adams, P. D. Davies, H. A. and Epstein, S. G. The Properties Of Liquid Metals, Taylor and Francis, 1966.

66) Arkharov, V. I. and Blankova, E. B. Fiz. Metal. Metalloved. 1959, 8, 87.

67) Wells, P. TRG. Mem. 2894(S) AGR/FESG/(65) P23, 1965.

68) Horsley, G. W. D.P. Report 36, 1961.

69) Kubaschewski, O. and Evans, E. Ll. Metallurgical Thermochemistry, Pergamon, 1958.

70) A.S.T.M. Powder Data File.

71) Pearson, W. B. A Handbook Of Lattice Spacings and Structures Of Metals and Alloys, Pergamon, 1958.

72) Mills, K. C. Private Communication, N.P.L.

73) Hultgren, R. et al. Selected Values Of Thermodynamic Properties Of Metals and Alloys, Wiley, 1963.

74) Batey, W. Private Communication, D.E.R.E.

75) Mott, B. W. Micro-Indentation Hardness Testing, Butterworths, 1956.

76) Bückle, H. Met. Rev. 1959, 4, 13.

77) Bückle, H. Metallforschg. 1946, 1, 47.

78) Belk, J. A. Private Communication, University Of Aston In Birmingham.

79) Vogel, A. I. Quantitative Inorganic Analysis, Longmans, 1942.

80) Dragan, I. M.Sc. Thesis, University Of Aston In Birmingham.

81) Hodierne, F. A. J.I.M. 1963, 91, 267.

82) Hughes, D. E. R. J.I.S.I. 1952, 170, 214.

83) Nicholson, A. Iron and Steel, 1964, 37, 290.

84) Hill, J. F. Met./31, University Of Aston In Birmingham, 1965.

85) Cottrell, A. H. The Mechanical Properties Of Matter, Wiley, 1964.

86) Tegart, W. J. M. Elements Of Mechanical Metallurgy, Collier-McMillan, 1966.

87) Oatley, C. W. Nixon, W. C. and Pease, R. F. W. Advances In Electronics and Electron Physics, 1965, 21, 181.

88) Asbury, F. E. and Baker, C. Metals and Mats. 1967, 1, 323.

89) Barnby, J. T. and Smith, E. Acta Met. 1964, 12, 1353.

90) Duhaj, P. and Ivan, J. J.I.S.I. 1968, 206, 1014.

91) Greenwald, S. Acta. Cryst. 1953, 6, 396.

92) Cheney, R. Hochgraf, F. G. and Spencer, C. W. Trans. A.I.M.E. 1961, 221, 492.

93) Darken, L. S. and Gurry, R. W. Physical Chemistry Of Metals, McGraw-Hill, 1953.

94) Le Claire, A. D. Progress In Metal Physics, Butterworths, 1949, 1953, 1, 4.

95) Shewmon, P. G. Diffusion In Solids, McGraw- Hill, 1963.

96) Cottrell, A. H. Introduction To Metallurgy, Arnold, 1965.

Table 1. Binary Iron-, Nickel-, Chromium-, Manganese- and Molybdenum-Tellurium Systems.*

System	β-phase	At% Te	Structure	γ-phase	At% Te	Structure	δ-phase	At% Te	Structure	ε-phase	At% Te	Structure
Fe-Te	β-range β-$FeTe_{0.9}$	44.44 -47.4 50	tetragonal a-3.819°A c-6.280°A	stable >750°C $FeTe_{1.1}$	52.5	unknown	δ-range δ-$FeTe_{1.5}$ stable>488°C	58.3- 60 60	hex a-3.816°A c-5.655°A c/a-1.482	ε-range ε-$FeTe_2$	66.1- 67.7 66.67	ortho a-6.240°A b-5.261°A c-3.872°A
Ni-Te	NiTe	50	hex a-3.980°A c-5.380°A c/a-1.350							$NiTe_2$	66.67	hex a-3.843°A c-5.265°A
Cr-Te	range CrTe	50-54 50	hex a-3.950°A c-6.160°A c/a-1.550	range $CrTe_{1.2}$ $CrTe_{1.3}$	54.55- 58.33 54.54 57.14	at 58.33 at% Te mono a-3.93°A b-6.09°A c-6.85°A β-91°5'	range $CrTe_{1.5}$	60- 66.7 60	hex a-3.92°A c-6.04°A c/a-1.54			
Mn-Te	range MnTe $MnTe_{1.01}$	50.29 - 61.78 50 50.29	hex a-4.132°A c-6.712°A c/a-1.624				$MnTe_{1.6}$	61.78		$MnTe_2$	66.67	cubic a-6.957°A
Mo-Te							$MoTe_{1.5}$	60	mono a-6.330°A b-3.469°A c-13.89°A	$MoTe_2$	66.67	hex a-3.518°A c-13.97°A c/a-3.970

* References 22,23,70,71.

Table 2. The Composition and Condition of A.I.S.I.316L Stainless Steel.

A.I.S.I.	COMPOSITION (WT.%)								
316L	Ni	Cr	Mo	C	Mn	Si	P	S	Fe
Specification	10-14	16-18	2-3	0.03 max	2.0 max	1.0 max	0.045 max	0.035 max	balance
Analysis	13.39	16.87	2.09	0.04	1.8	0.59	0.04	0.038	balance

MECHANICAL PROPERTIES (SOLUTION TREATED ALLOY) (35)				
Condition	Tube Size	U.T.S.(tons.ins.$^{-2}$)	Elongation(%)	Hardness(B.H.N.)
20% C.W.	0.200" i/d 0.015" w/t	33.5	50	150

Table 3. Some of The Physical Properties of Tellurium.

Atomic No.	Atomic Wt.	M.pt.(°C)	B.pt.(°C)	S.G.(20°C)
52	127.6	450	1,390	6.25

Table 4. Etching Reagents.

Etchant	Use
4grms. $CuSO_4$, 20ml. HCl, 20ml. H_2O.	Reveals austenite grain boundaries.
5grms. $CuCl_2$, 100ml. HCl, 100ml. H_2O, 100ml. ethyl alcohol.	Reveals austenite grain boundaries.
50% aqua regia, 50% glycerol.	Reveals austenite grain boundaries.
45grms. citric acid, 30grms. KI, 6ml. HCl, made upto 90ml. with H_2O. Stainless steel cathode. 2 volts.	Attacks austenite and allows the determination of a second phase, eg. α, σ, $M_{23}C_6$. Used for carbon extraction replicas.
1 part HNO_3, 1 part HCl, 2 parts glycerol.	Attacks austenite lightly revealing the presence of a second phase, eg. α,σ heavily attacked, $M_{23}C_6$ outlined, corrosion product left proud. Used for carbon replicas.
10% HCl in alcohol. Stainless steel cathode. 9 volts.	Attacks austenite leaving the second phase proud, eg. $M_{23}C_6$, corrosion product. Used for carbon extraction replicas.
10% KOH. Stainless steel cathode. 2 volts.	Outlines the second phase, eg. α yellow, σ deep yellow, α' pale blue and $M_{23}C_6$ pale yellow after σ and α.
10% oxalic acid. Stainless steel cathode. 2-3 volts.	Reveals austenite grain boundaries and outlines the second phase, eg. α, σ and $M_{23}C_6$.
30grms. KOH, 30grms. potassium ferricyanide, 60ml. H_2O.	Reveals austenite grain boundaries and the presence of a second phase, eg. σ.

Table 5. The Interplanar Spacings Of Tellurium.

Observed d(°A)	A.S.T.M. d(°A)
3.150	3.860
2.310	3.230
2.200	2.351
2.060	2.087
1.950	1.980
-	1.930
1.830	1.835
-	1.781
-	1.758
1.600	1.616
1.470	1.479
-	1.459
1.410	1.417
1.370	1.383
1.300	1.309
-	1.287
-	1.257
-	1.234
-	1.180
1.170	1.174
1.130	1.133
-	1.095
-	1.078
-	1.070
-	1.053
1.040	1.043
-	1.039
1.010	1.010
-	1.007

A.S.T.M. d(°A)	3.23	2.35	2.23	3.86
A.S.T.M. I/I$_1$	100	37	31	20
Observed d(°A)	3.15	2.31	2.19	-
Observed I	1	2	3	-

Table 6. The Interplanar Spacings Of The Corrosion Products.

A.S.T.M. d(°A) β-$FeTe_{0.9}$	Observed d(°A) A.I.S.I.316L-Te	Observed d(°A) Fe-Te
6.270	-	-
3.260	3.245	3.243
3.140	3.109	3.099
2.708	2.698	-
2.483	2.473	-
2.428	-	-
2.094	2.094	2.080
2.047	2.033	2.033
1.912	1.902	1.909
1.836	1.816	1.823
1.650	1.643	1.644
1.634	1.610	-
1.570	1.551	1.560
1.484	-	-
1.452	1.436	1.440
1.412	1.403	1.407
1.352	1.356	1.348
1.312	1.316	1.319
1.248	-	1.247
1.241	1.242	-
1.213	-	-
1.210	1.205	1.208
1.193	-	-
1.186	1.181	1.187
1.156	1.150	1.152
1.139*	-	1.135
1.136	-	-
1.128*	1.127	1.125
1.088	-	-
1.049	-	1.046
1.045*	-	-
1.024*	-	1.022
1.012	-	-
1.009*	-	-
1.004	-	1.005

*high intensity lines due to absorption.

A.S.T.M. d(°A) A.S.T.M. I/I_1	β-$FeTe_{0.9}$	2.050 100	3.260 80	1.650 70	6.270 10
Observed d(°A) Observed I	A.I.S.I.316L -Te	2.033 1	3.245 2	1.634 3	- -
Observed d(°A) Observed I	Fe-Te	2.033 1	3.240 2	1.644 2	- -

Table 7. The Weight Of The Torsion Test Specimens Before And After Exposu

Specimen No.	Temperature(°C)	Exposure Time(h-mins)	Weight(grm) Before	After	Weight Change
1-6	650	1-10	21.6886	21.6894	+0.0008
2-6	650	2-5	21.1818	21.6894	+0.0005
3-6	650	4-1	21.8674	21.8679	+0.0005
4-6	650	7-4	21.8469	21.8474	+0.0005
5-6	650	16-20	21.9846	21.9850	+0.0004
6-6	650	32-6	22.1570	22.1575	+0.0005
7-6	650	64-6	22.3223	22.3227	+0.0004
8-6	650	127-1	22.1211	22.1220	+0.0009
9-6	650	239-41	22.3329	22.3330	+0.0001
10-6	650	527-33	22.3654	22.3652	-0.0002
11-6	650	1,072-30	22.1174	22.1170	-0.0004
Controls					
1-6-C	650	1-10	10.1672	10.1679	+0.0007
2-6-C	650	4-1	10.3164	10.3166	+0.0002
3-6-C	650	16-20	9.2864	9.2873	+0.0009
4-6-C	650	64-6	9.7568	9.7574	+0.0006
5-6-C	650	239-41	9.9552	9.9558	+0.0006
6-6-C	650	1,072-30	10.1263	10.1271	+0.0008
1-7	750	1-0	21.9122	21.9127	+0.0005
2-7	750	2-3	22.2488	22.2492	+0.0004
3-7	750	4-0	21.1291	21.1305	+0.0014
4-7	750	7-4	21.9905	21.9917	+0.0012
5-7	750	16-10	21.7448	21.7452	+0.0004
6-7	750	32-8	22.2460	22.2460	+0.0002
7-7	750	64-0	22.4542	22.4544	+0.0002
8-7	750	127-0	22.5541	22.5545	+0.0004
9-7	750	239-25	22.2632	22.2632	0.0000
10-7	750	527-25	22.2287	22.2289	+0.0002
11-7	750	1,072-30	22.5283	22.5282	-0.0001
Controls					
1-7-C	750	1-0	10.0160	10.0169	+0.0009
2-7-C	750	4-0	10.0638	10.0642	+0.0004
3-7-C	750	16-10	10.1501	10.1510	+0.0009
4-7-C	750	64-0	9.3460	9.3464	+0.0004
5-7-C	750	239-25	10.0916	10.0920	+0.0004
6-7-C	750	1,072-30	10.4772	10.4764	-0.0008

Table 8. The Rate Of Penetration Of Liquid Tellurium In A.I.S.I.316L Austenitic Stainless Steel.

A. 0.45 grms. Te 650°C.

Specimen	Exposure (h-mins)	Intergranular Penetration Depth (μ)	Intergranular Penetration Rate ($\mu.hr^{-1}$)	Transgranular Penetration Depth (μ)	Transgranular Penetration Rate ($\mu.hr^{-1}$)
LT16	240	77.25	0.3219	27.27	0.1136
- 26	500	93.00	0.1860	42.50	0.0850
- 36	1,001	107.00	0.1069	51.00	0.0509
- 46	2,009	122.90	0.0612	51.00	0.0254
- 56	4,025	159.50	0.0396	52.90	0.0131
- 66	6,016	170.00	0.0283	53.50	0.0089
- 76	8,227	160.00	0.0194	58.75	0.0071
- 86	10,049	170.00	0.0174	51.00	0.0051
B. 0.45 grms. Te 750°C.					
LT17	240	174.75	0.7280	54.00	0.1202
- 27	500	205.00	0.4101	60.15	0.2250
- 37	1,001	247.75	0.2474	65.40	0.0653
- 47	2,009	279.00	0.1389	52.50	0.0261
- 57	4,026	280.00	0.0696	53.35	0.0132
- 67	5,825	282.50	0.0485	56.25	0.0097
- 77	7,982	279.50	0.0349	57.50	0.0072
- 87	9,924	287.50	0.0289	-	-
C. Te rod 650°C.					
LT16	1-10	-	-	20.00	17.1700
- 26	2-5	-	-	25.00	12.0000
- 36	4-1	-	-	40.00	10.0000
- 46	7-4	-	-	50.00	7.0760
- 56	16-20	-	-	55.00	3.3680
- 66	32-6	-	-	52.50	1.6360
- 76	64-6	138.00	2.1530	128.00	1.9960
- 86	127-1	177.50	1.3970	162.50	1.2790
- 96	239-41	230.00	0.9590	210.00	0.8760
- 10 6	527-33	265.00	0.5020	215.00	0.4080
- 11 6	1,072-30	320.00	0.2980	237.50	0.2210
D. Te rod 750°C.					
LT17	1-0	-	-	45.00	45.0000
- 27	2-3	-	-	47.50	23.1700
- 37	4-0	-	-	60.00	15.0000
- 47	7-4	-	-	93.75	13.2600
- 57	16-10	-	-	133.75	8.2750
- 67	32-8	-	-	165.00	5.1360
- 77	64-0	-	-	212.50	3.3200
- 87	127-0	230.00	1.8110	167.50	1.3200
- 97	239-25	310.00	1.2950	225.00	0.9400
- 10 7	527-25	351.50	0.6660	200.00	0.3790
- 11 7	1,072-30	415.00	0.3870	275.00	0.2560

Table 9. The % Penetration By Liquid Tellurium And % Reduction In Shear Stress (at yield) And Total Ductility (revolutions to failure) For The Torsion Test Specimens.

Specimen	Penetration (%)		Reduction (%)	
	Trans-	Intergranular	Stress	Ductility
1-6	4.0	-	18.4	50.7
2-6	4.9	-	20.0	57.5
3-6	7.9	-	22.0	63.0
4-6	9.9	-	25.3	62.0
5-6	10.9	-	25.3	62.0
6-6	10.3	-	31.0	59.0
7-6	25.1	27.2	34.5	69.0
8-6	31.8	34.8	36.5	63.0
9-6	41.2	45.2	38.4	74.0
10-6	42.4	52.2	51.0	72.0
11-6	47.0	63.0	55.0	87.5
1-7	8.9	-	-	-
2-7	9.3	-	36.5	60.5
3-7	11.8	-	49.2	42.0
4-7	18.4	-	40.1	71.0
5-7	26.2	-	60.8	67.0
6-7	32.5	-	53.0	81.5
7-7	41.7	-	78.0	77.0
8-7	32.9	45.2	78.5	-
9-7	44.2	61.0	92.5	88.0
10-7	39.2	69.0	-	-
11-7	54.0	82.0	-	-

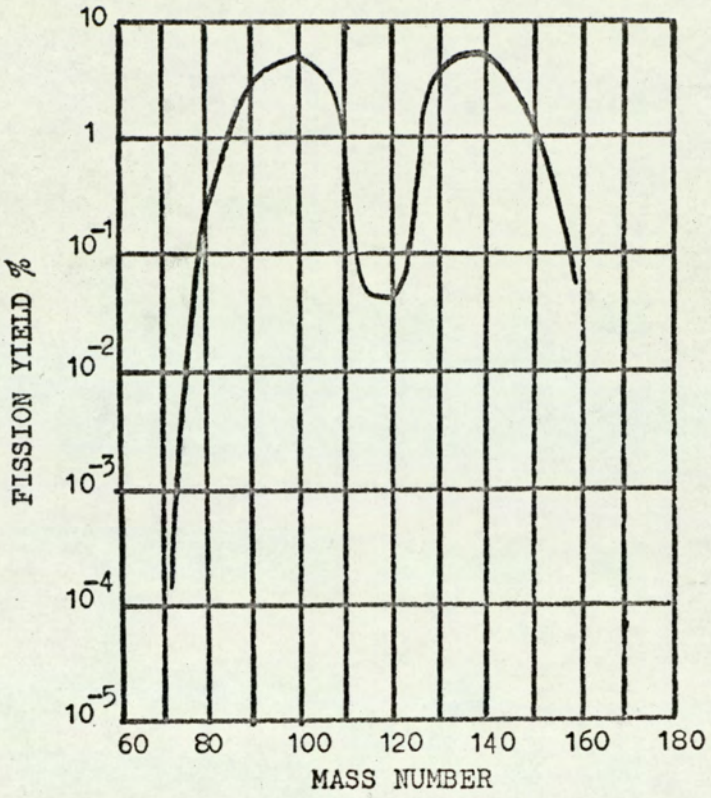

Fig.1 The Fission Product Yield For Pu^{239}(1).

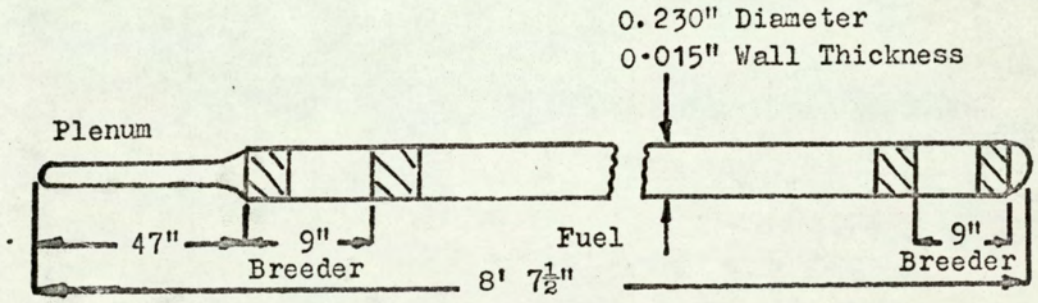

Fig.2 The Fuel Pin For The Prototype Fast Reactor(11).
(not to scale)

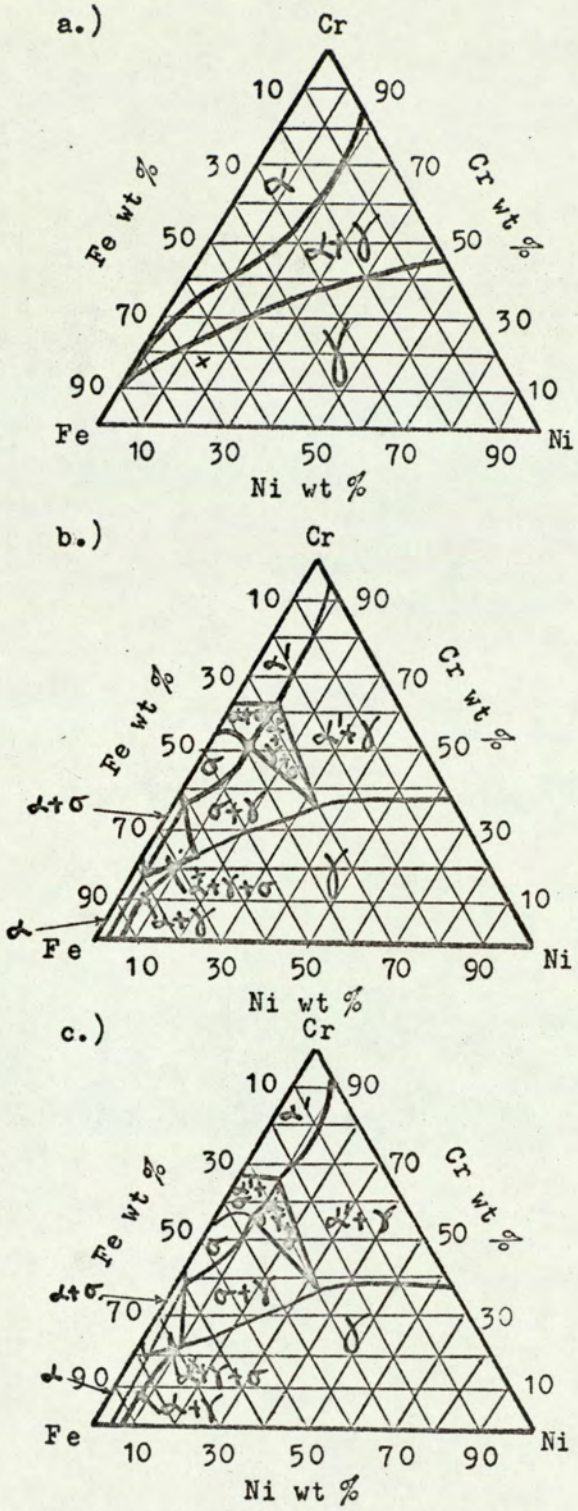

Fig.3 Isothermal Sections Of The Fe-Ni-Cr System At a.) 1200°C, b.) 800°C, and c.) 650°C. (25, 26)

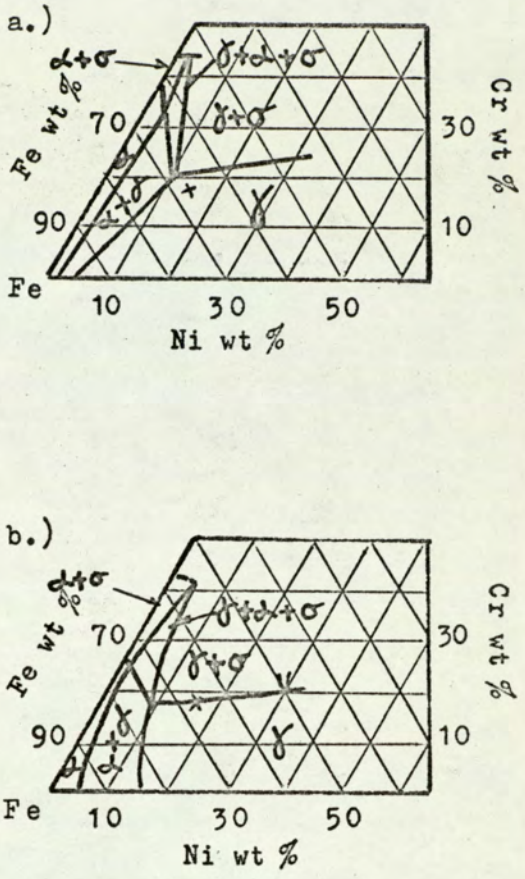

Fig.4 Isothermal Sections Of The Fe-Ni-Cr System At a.) 800°C and b.) 650°C. (27)

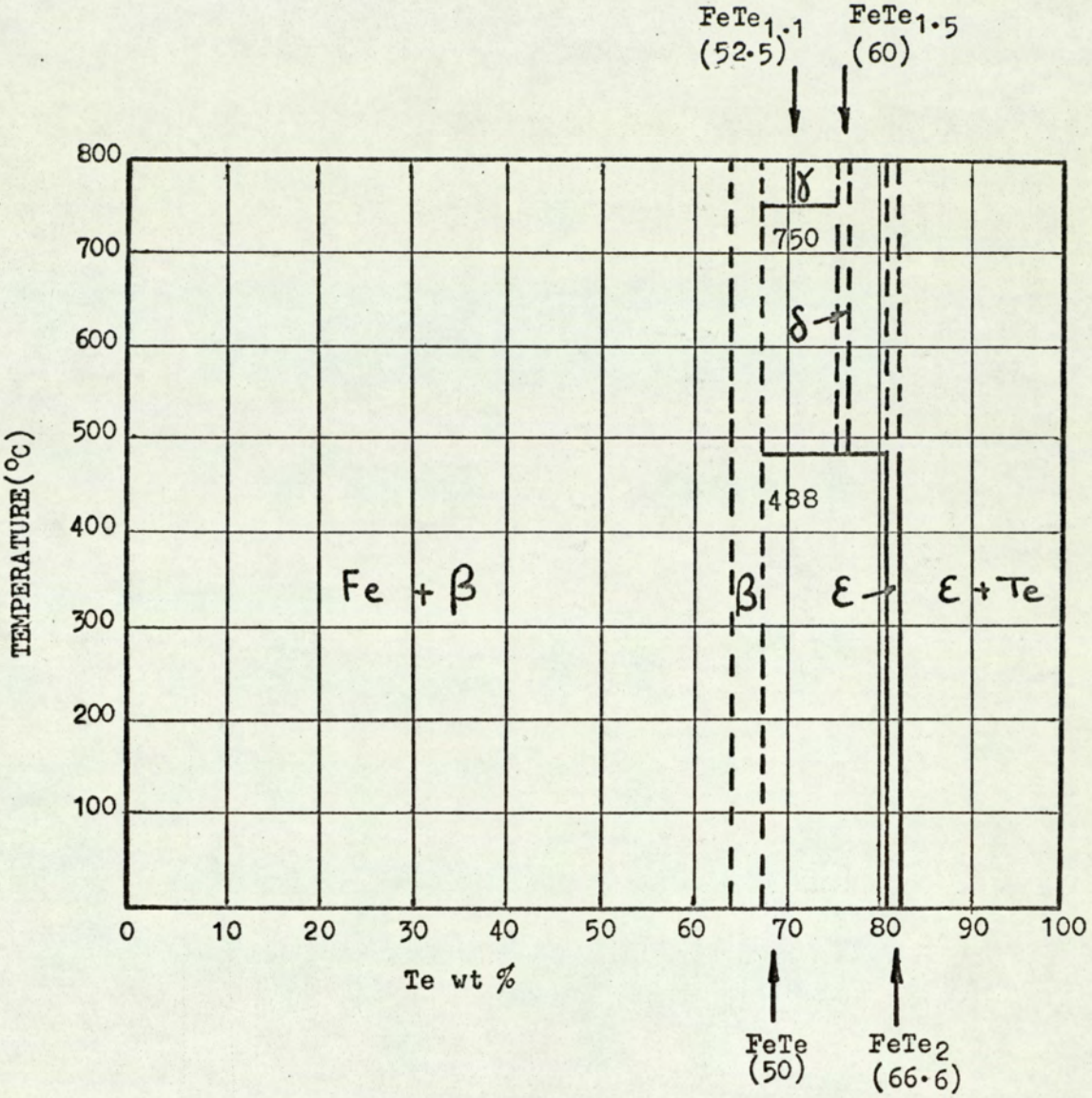

Fig.5 The Binary Fe-Te System(22,23,70,71).
(at% in brackets)

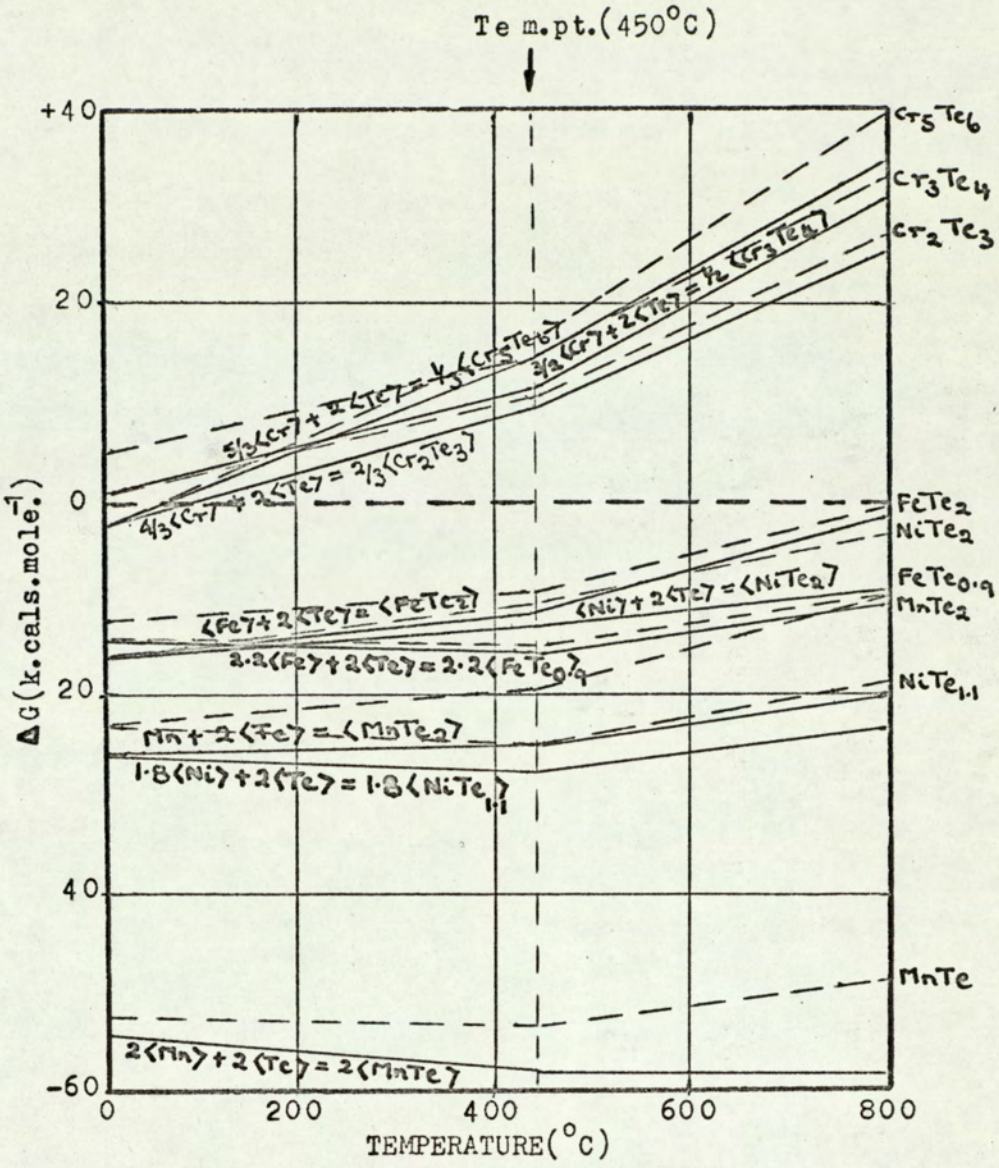

Fig. 6 The Free Energy of Formation of the Transition Metal Tellurides.

Fig.7 A Welded Compatibility Couple.

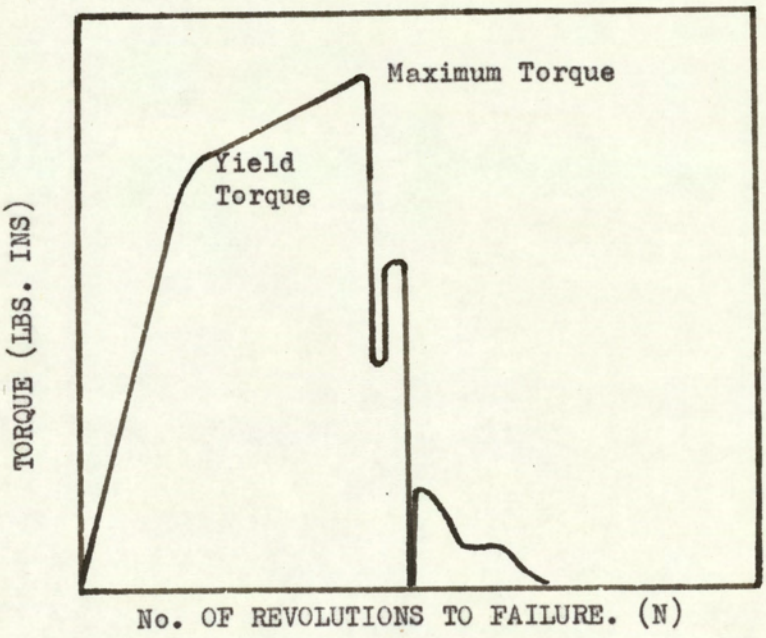

Fig.9 Torsion Test Curve.

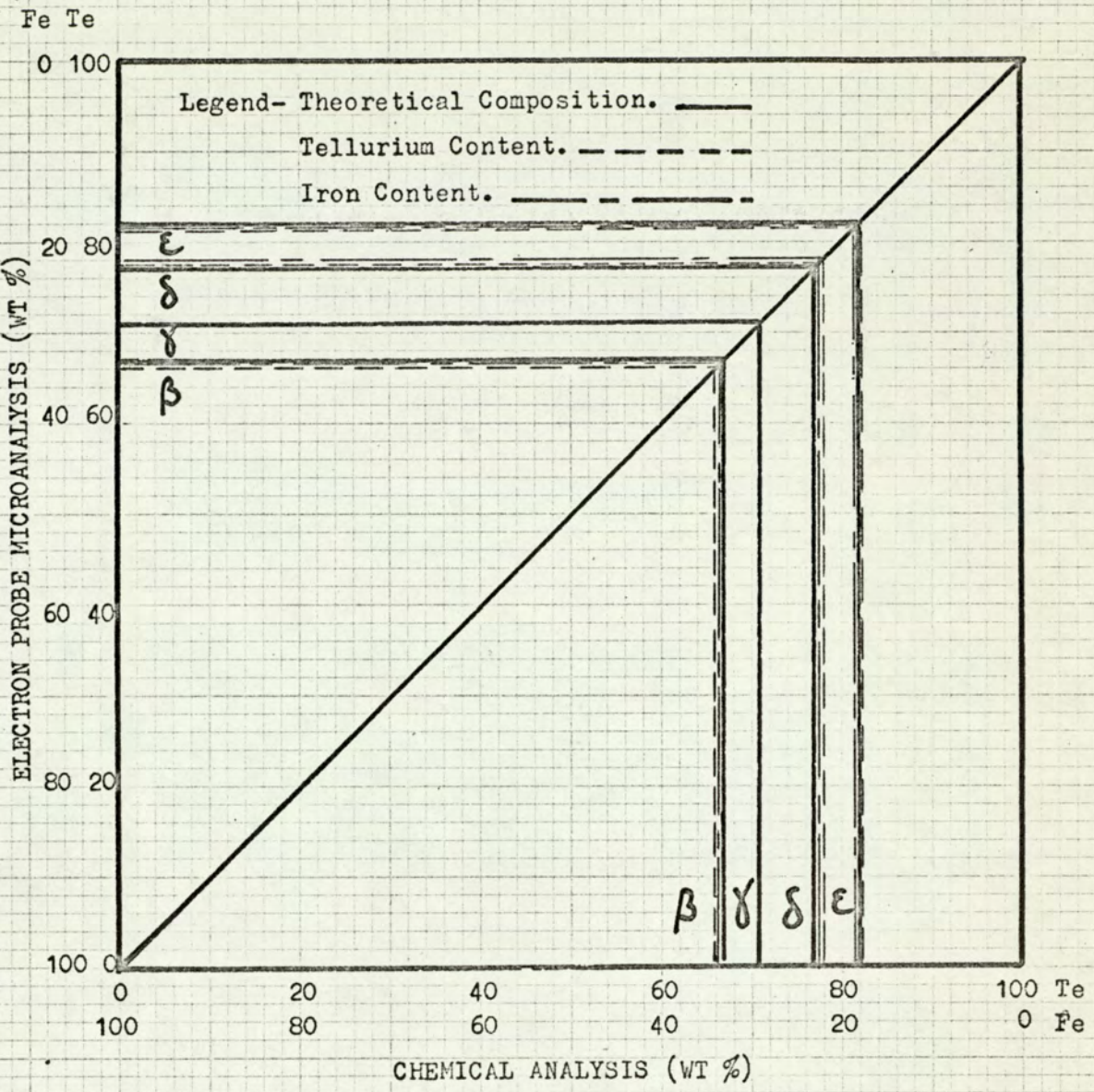

Fig.8 Comparison Of The Chemical And Electron Probe Microanalysis Results For The Synthetic Iron Tellurides.

Fig. 10a) Initial wetting of the stainless steel surface after contact with liquid tellurium for 70 minutes. Unetched 200x.

Fig. 10b) Transgranular penetration by the liquid into the alloy after 4 hours exposure. Unetched 200x.

Fig. 10c) Increased transgranular penetration after 32 hours exposure with a 'secondary' penetration (see text). Unetched 200x.

Fig. 10d) Extensive transgranular penetration after exposure to liquid tellurium for 127 hours. Unetched 200x.

Fig. 10e) The corroded interface etched after 527 hours exposure. Etched electrolytic 10 wt % oxalic acid 350x.

Fig. 10f) The two regions of liquid tellurium penetration after 1,072.5 hours exposure. Unetched 200x.

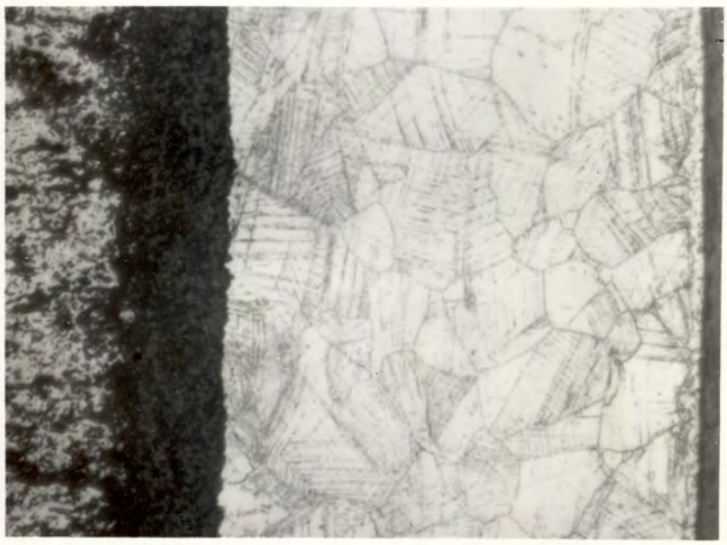

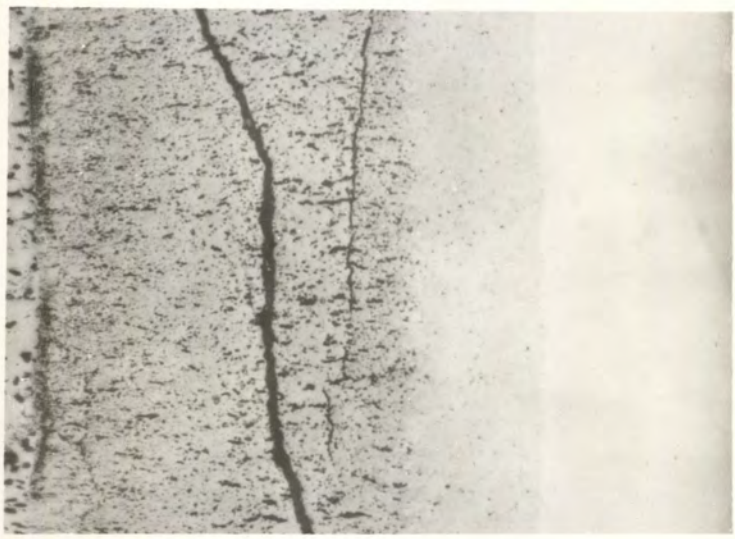

Fig. 11a) Initial transgranular penetration of the liquid phase into the alloy surface after 4 hours exposure. Unetched 200x.

Fig. 11b) Extensive transgranular penetration after 16 hours exposure. Unetched 200x.

Fig. 11c) Trans- and intergranular penetration of liquid tellurium into the stainless steel after contact for 239.5 hours. Unetched 200x.

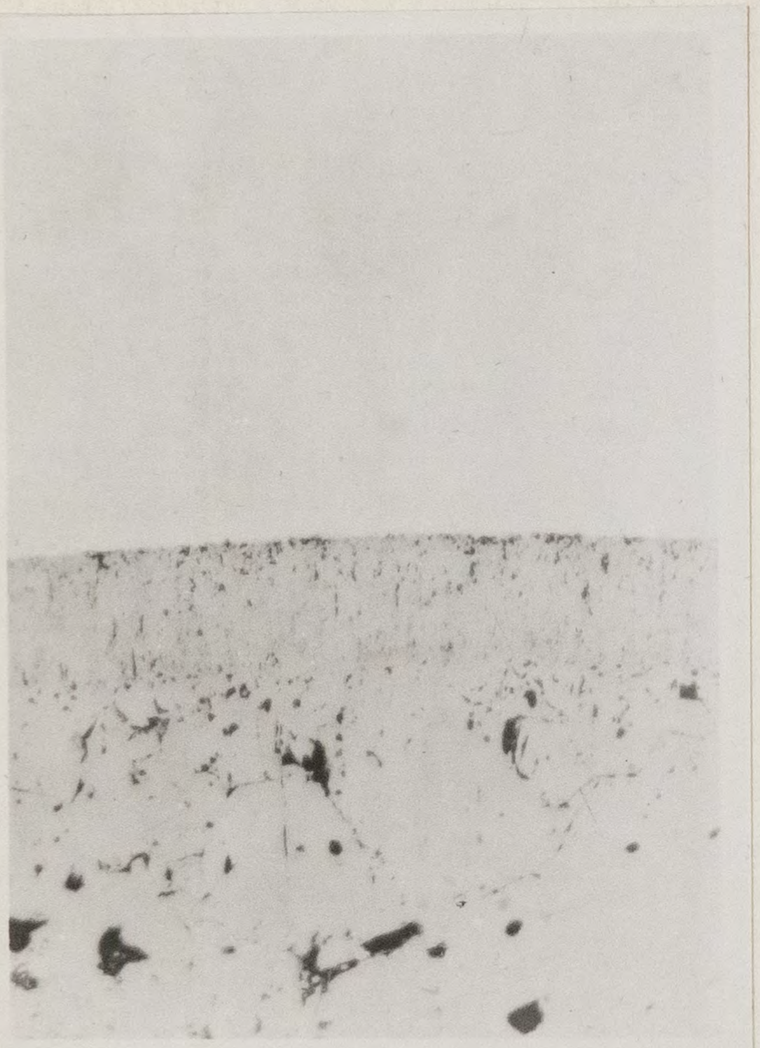

Fig. 11d) Extensive intergranular penetration after 527.5 hours exposure. Unetched 200x.

Fig. 11e) Complete intergranular penetration after 1,072.5 hours exposure. Unetched 200x.

Fig. 11f) High contrast in the corroded region after 239.5 hours exposure. Etched electrolytic 10 wt % oxalic acid 350x.

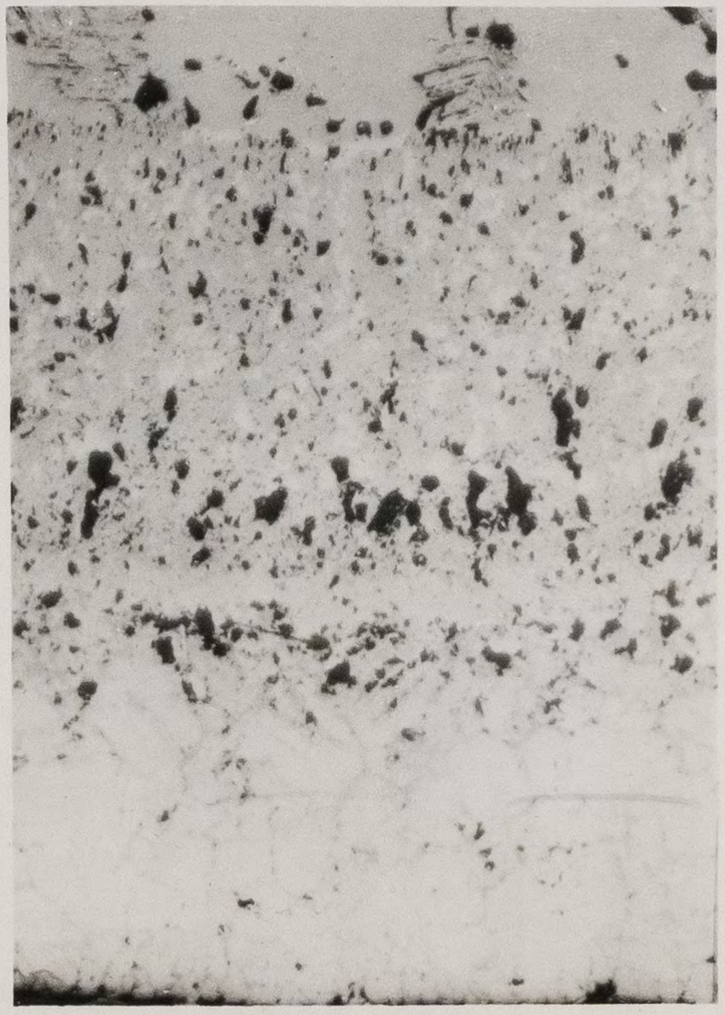

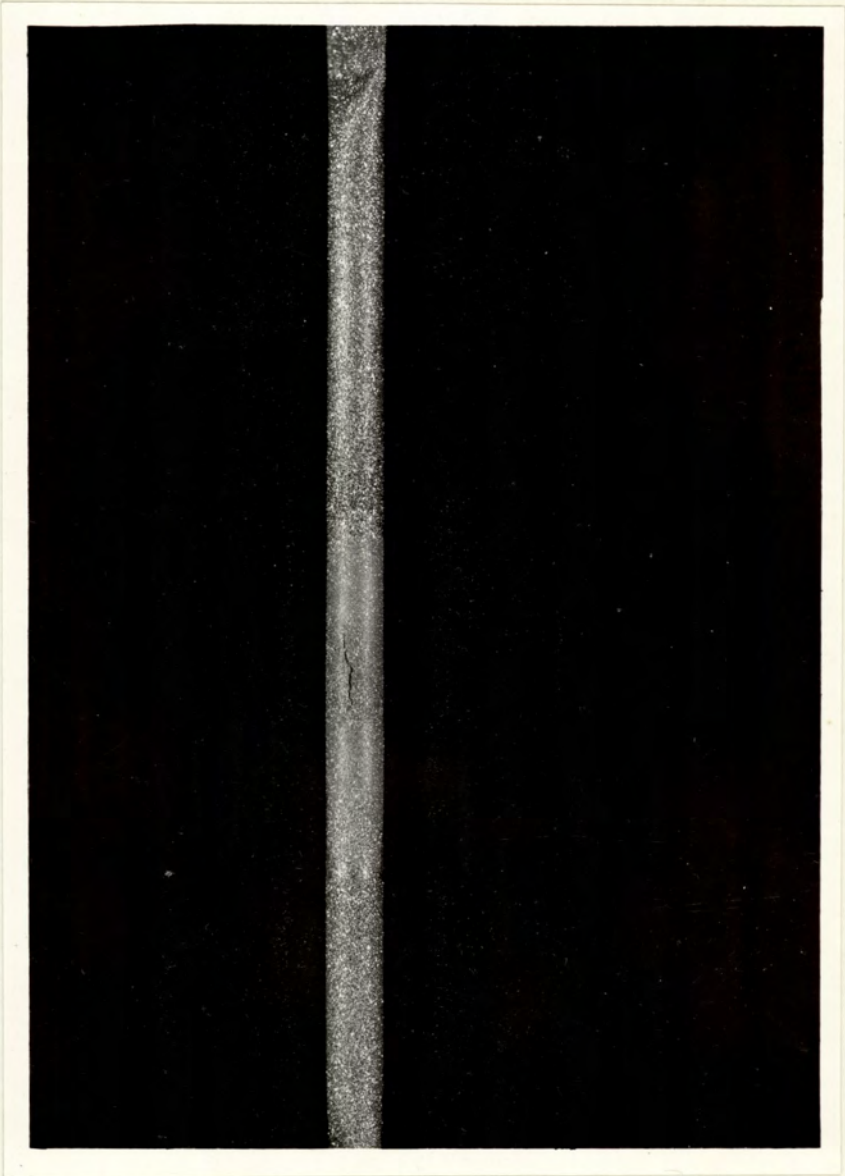

Fig.12 Complete Corrosion Of The A.I.S.I.316L Stainless Steel After 1,072.5 Hours Exposure At 750°C To Liquid Tellurium.

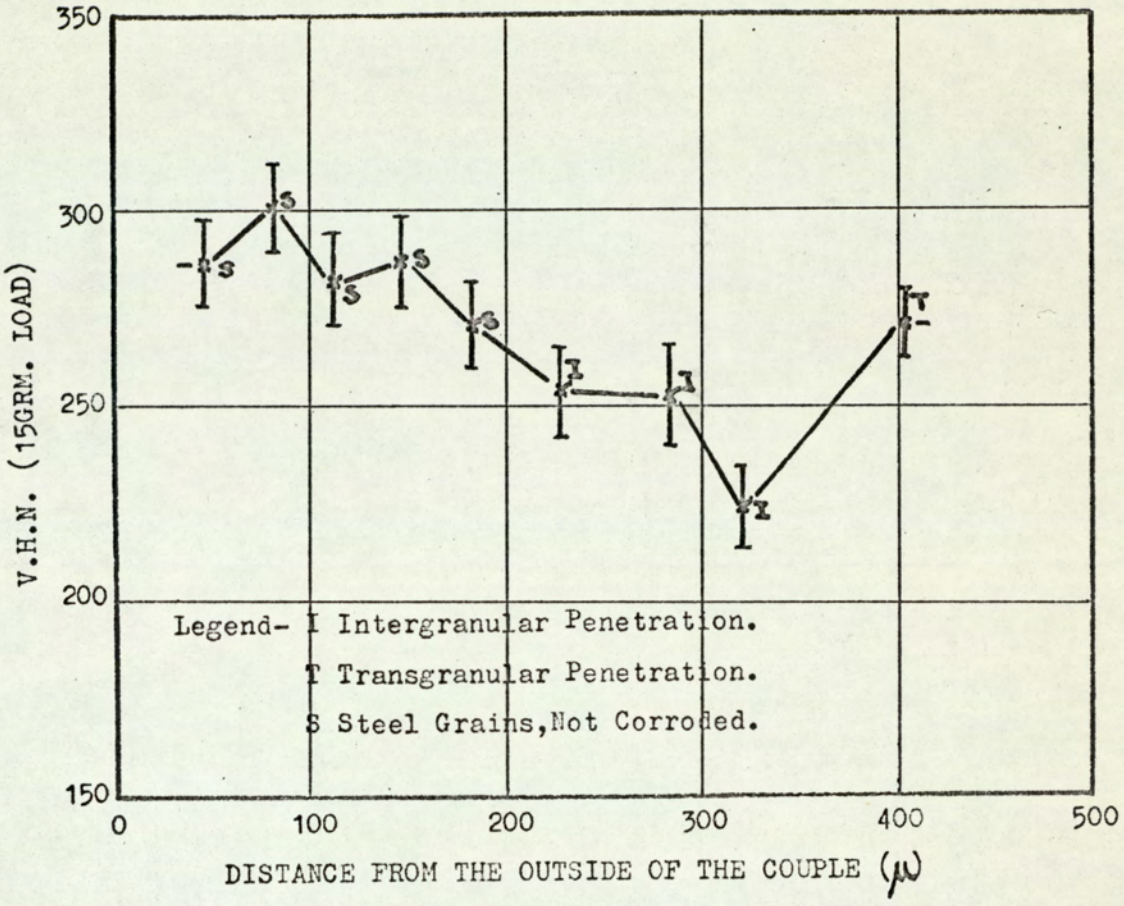

Fig.13 The Variation In Microhardness Across A Corroded Couple.

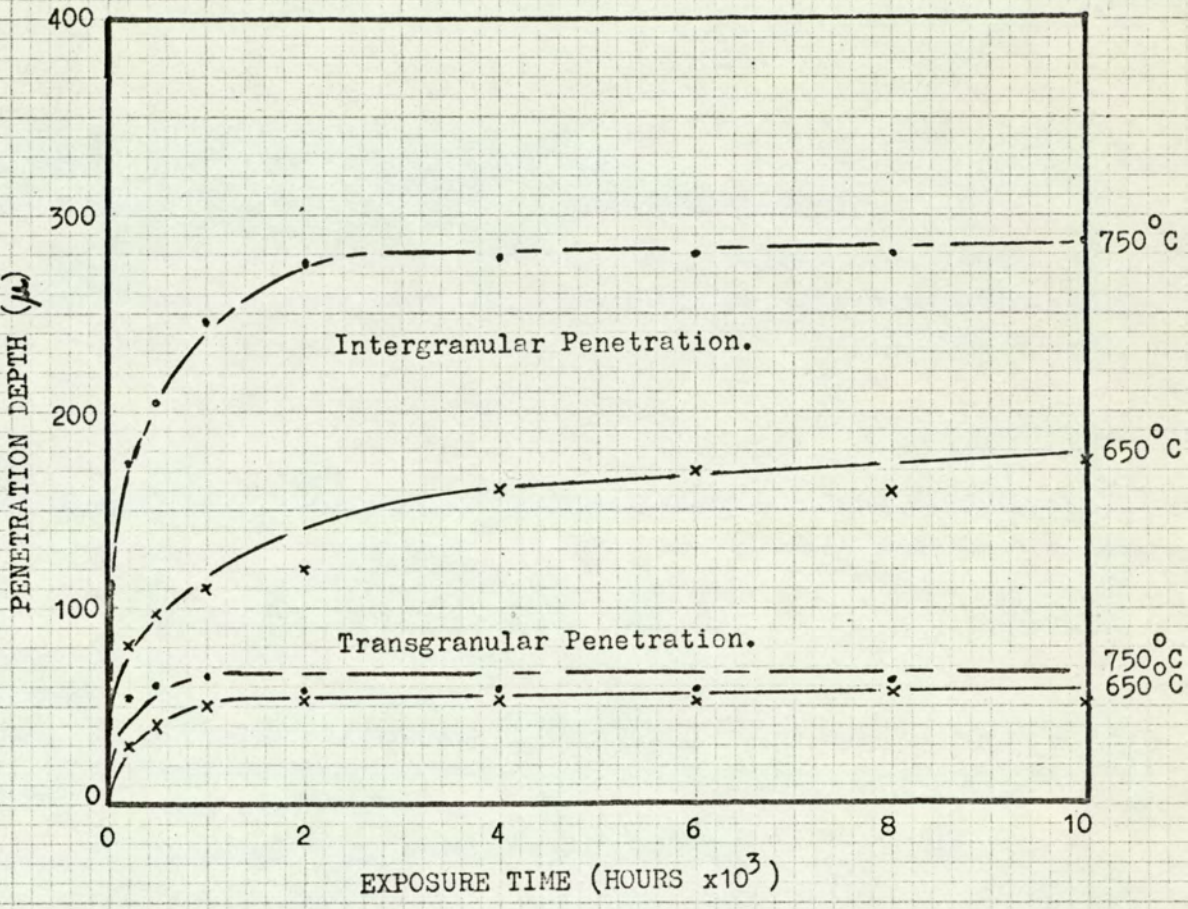

Fig.14 The Depth Of Penetration As A Function Of Exposure Time At 650°C and 750°C (0.45 grms. Te)

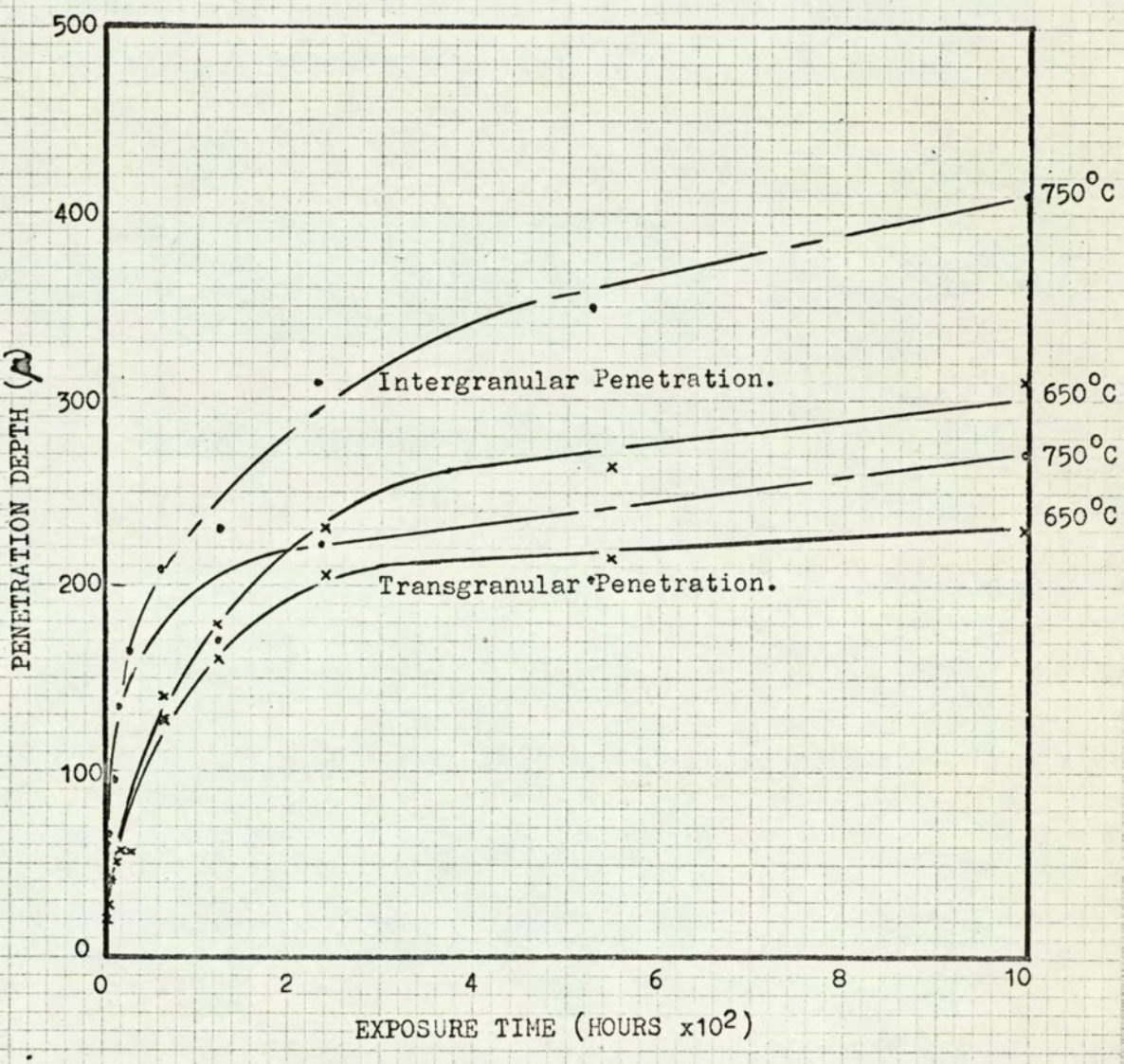

Fig.15 The Depth Of Penetration As A Function Of Exposure Time At 650°C and 750°C (Te Rod)

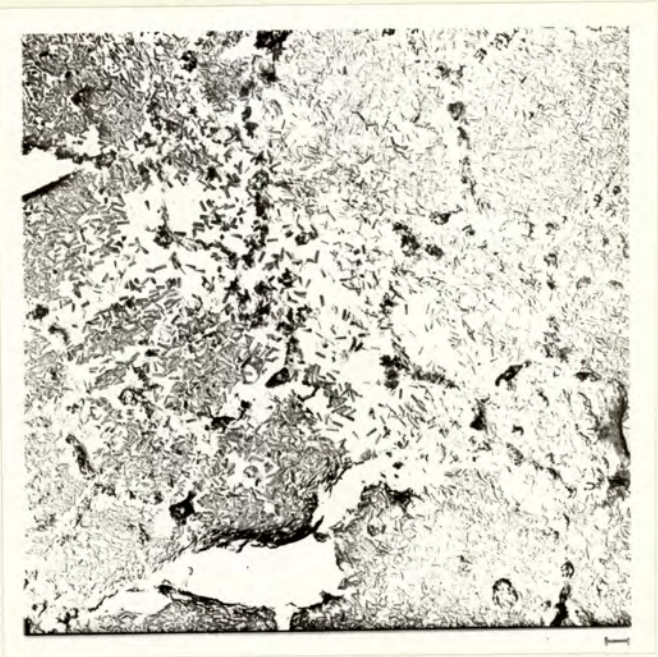

Fig. 16a) Two-stage Carbon Replica Showing Grain Boundary Carbide And Transgranular Precipitation. 2,500x.

Fig. 16b) Two-stage Carbon Replica Showing Precipitate At A Triple Point In The Corroded Area. 13,000x.

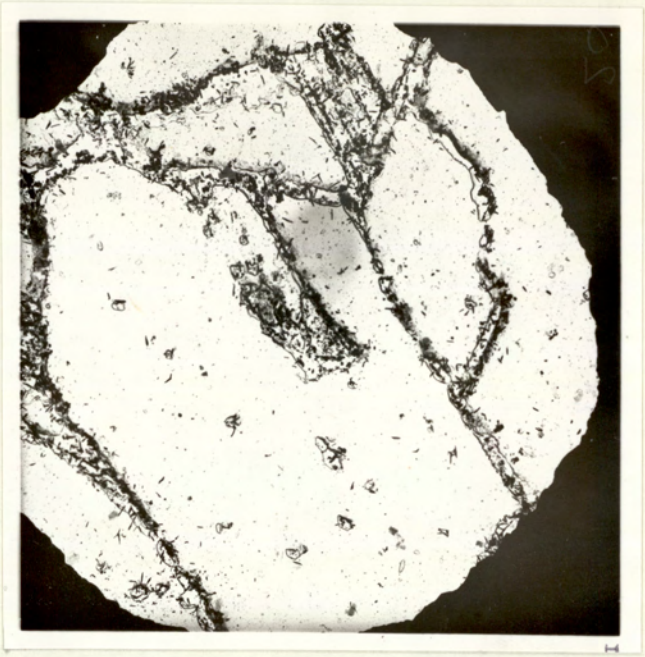

Fig.17 Trans- and Intergranular Precipitated Carbide In The Stainless Steel. 1,000x.

a) 55,000x.

b) 55,000x.

c)

Fig.18 a) Bright Field Micrograph, b) Dark Field Micrograph and c) Electron Diffraction Pattern Taken Of The Precipitate In Fig.17.

a) 55,000x.

b)

Fig.19 a) Carbon Extraction Replica and b) Electron Diffraction Pattern Of The Precipitate In Fig.16.

Fig.20 Analysis Of

A Couple After

1,500 Hours At 650°C.

Legend.

Te L_α ——————

Fe K_α – – – – –

Ni K_α — — —

Cr K_α —— – ——

Mn K_α —— – – ——

Mo K_α – – – – –

With Analysis In Similar Order. Applies To All Such Subsequent Figures.

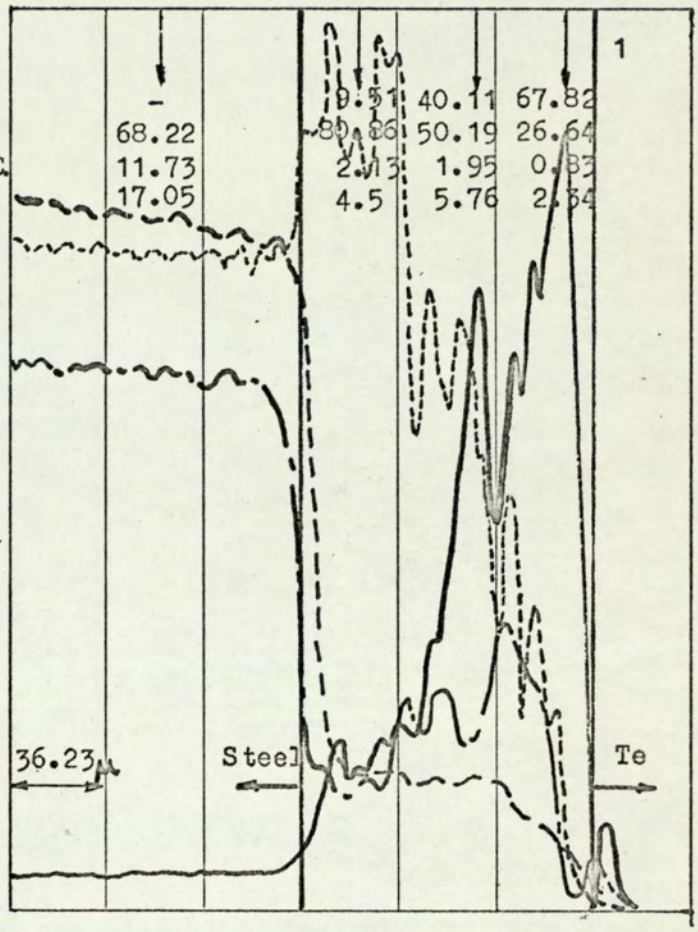

Fig.21 Intergranular Penetration After 1,500 Hours At 750°C.

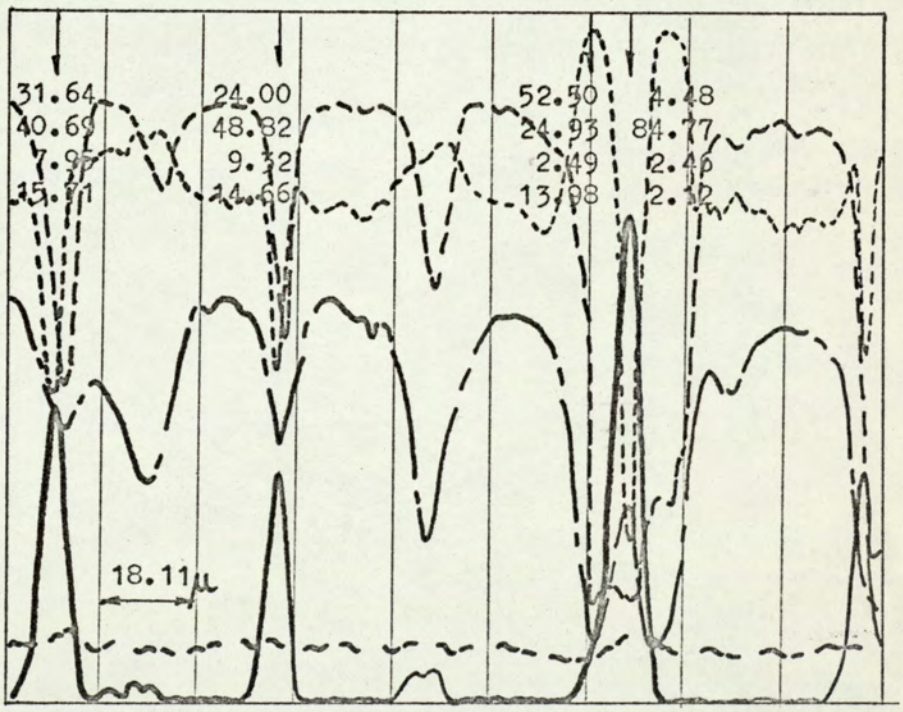

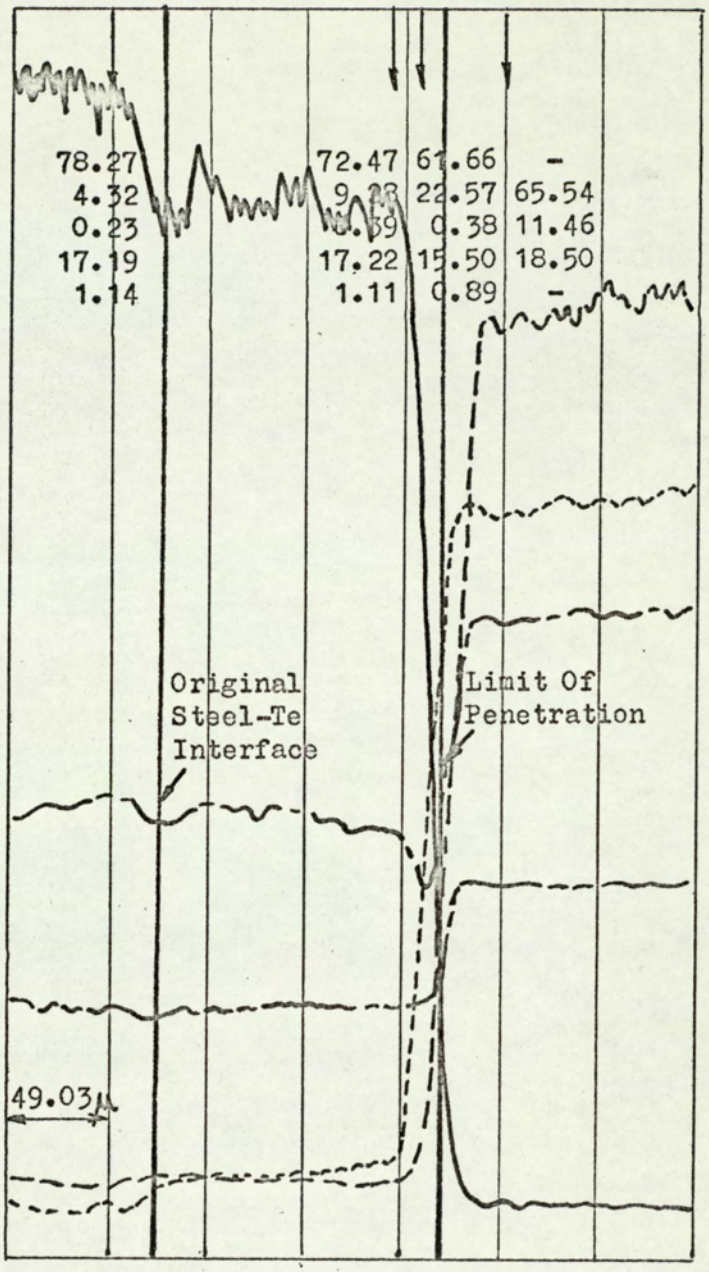

Fig.22 Analysis Of A Couple After 16 Hours Exposure At 750°C.

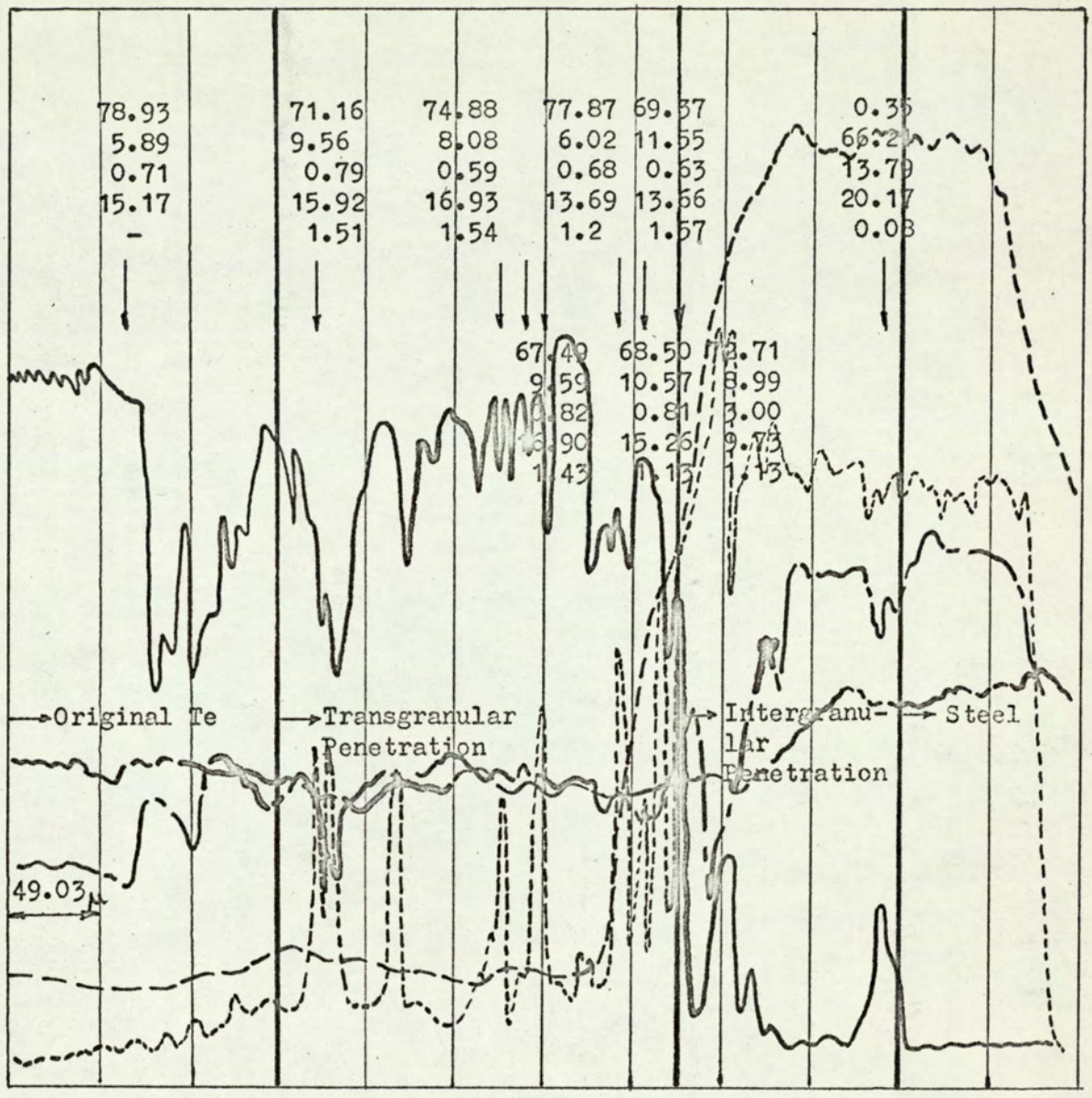

Fig.23 Analysis Of A Couple After 239.5 Hours Exposure At 750°C.

a) Electron Image.

Fig.24 Electron and X-ray Micrographs Illustrating The Distribution Of Te, Fe, Ni and Cr At The Reaction Interface. 170x.

b) Te L_{α} X-ray.

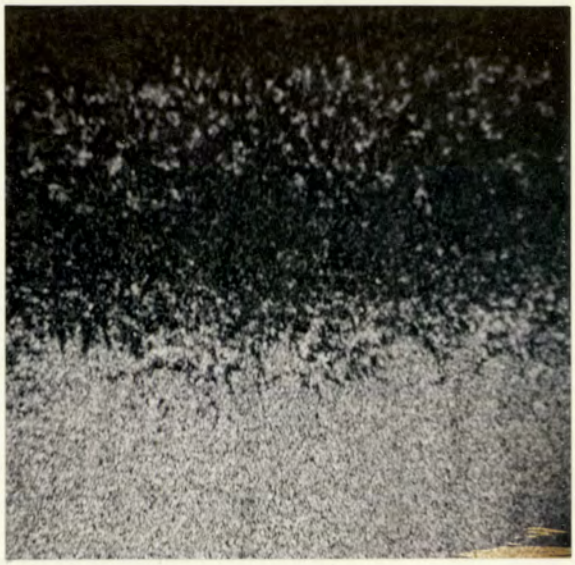

c) Fe K_{α} X-ray.

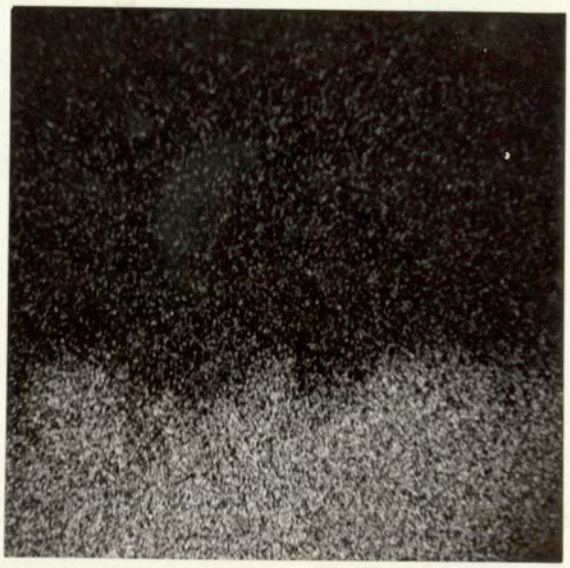

d) Ni K_{α} X-ray.

e) Cr K_{α} X-ray.

a) Electron Image.

Fig.25 Electron and X-ray Micrographs Showing Te Concentration and Fe, Ni and Cr Depletion In The Grain Boundaries Of The Alloy. 780x.

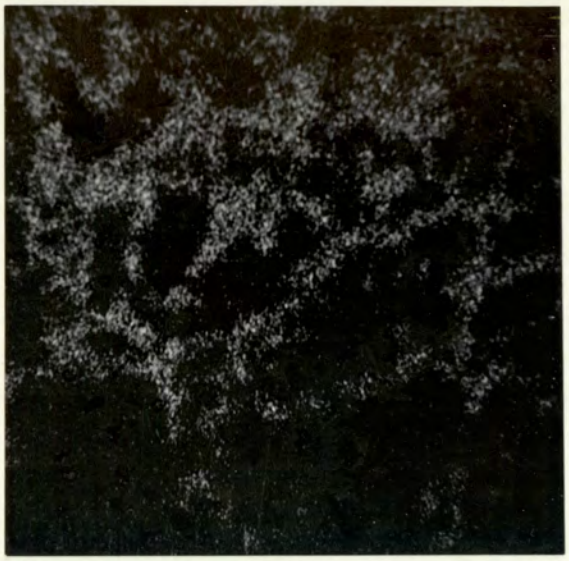

b) Te L_{α} X-ray.

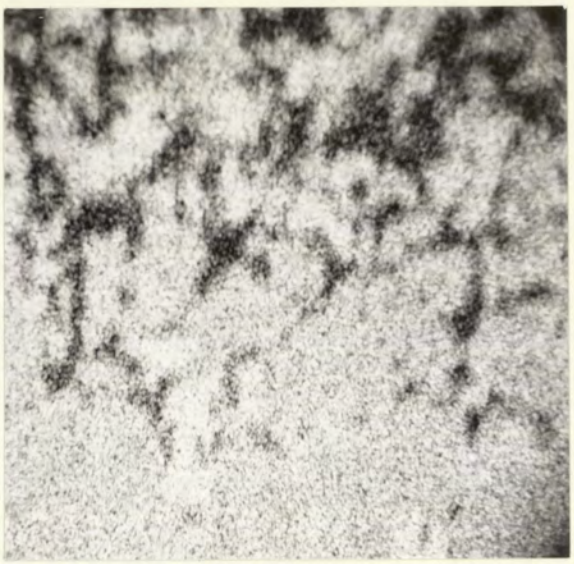

c) Fe K_{α} X-ray.

d) Ni K_{α} X-ray.

e) Cr K_{α} X-ray.

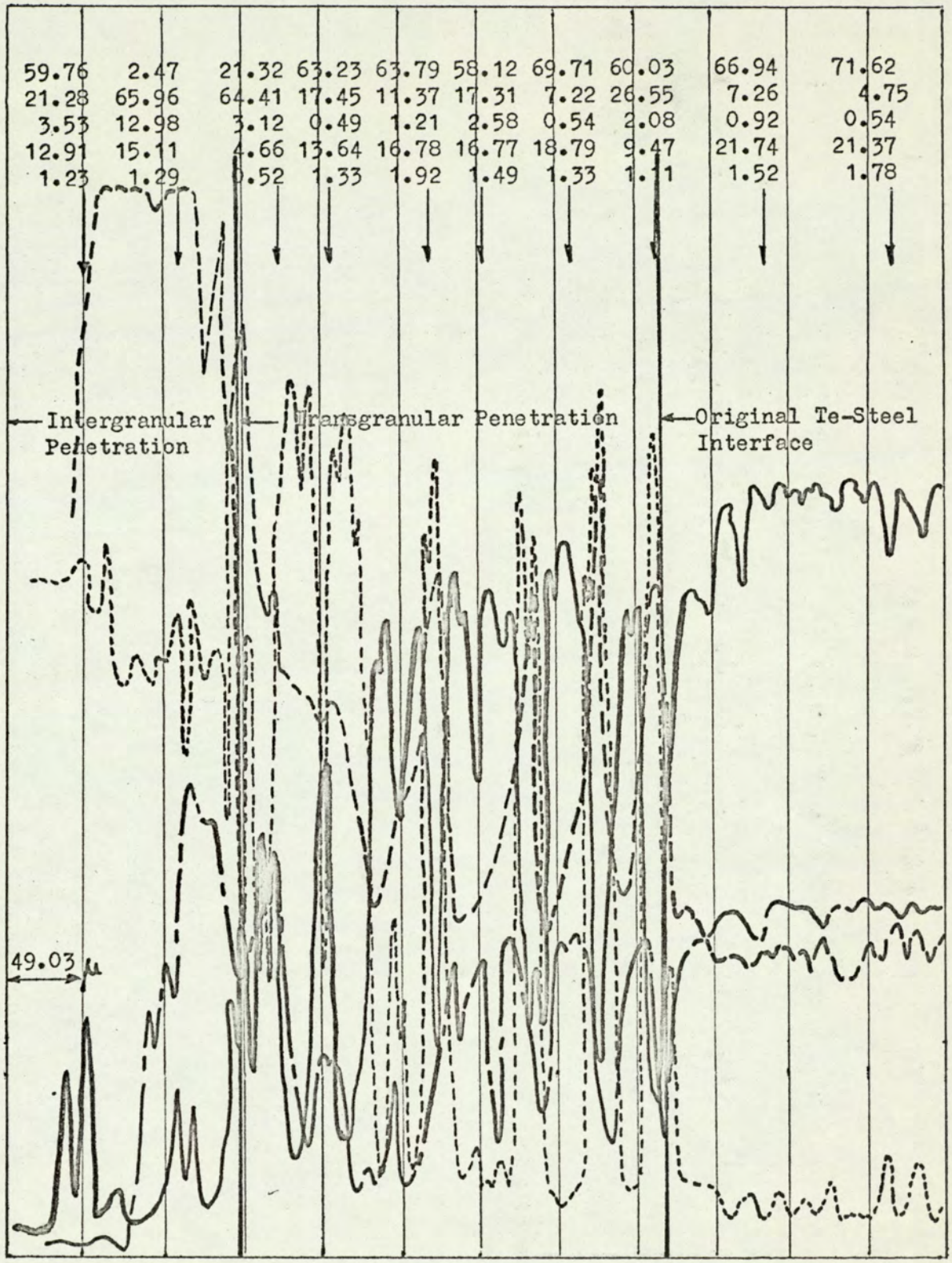

Fig.26 Analysis Of A Couple Showing Complete Grain Boundary Penetration Of The Alloy.

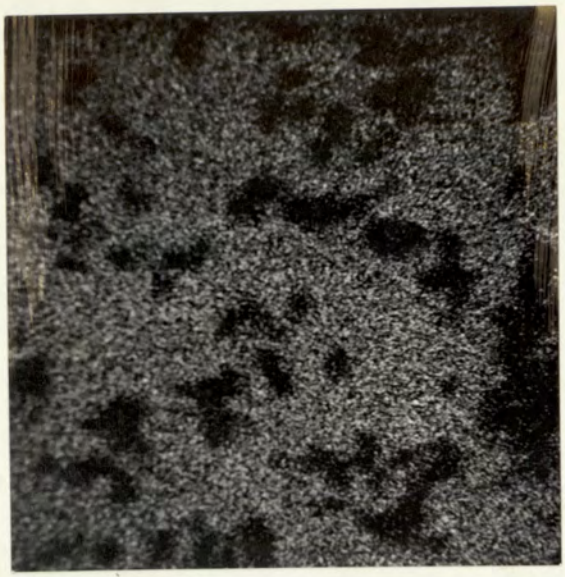

a) Te L_{α} X-ray.

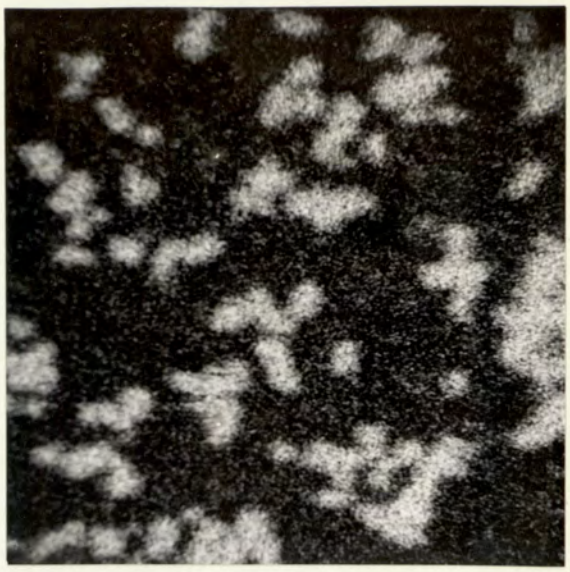

b) Fe K_{α} X-ray.

c) Ni K_{α} X-ray.

d) Cr K_{α} X-ray.

Fig.27 X-ray Micrographs Showing A Region Of Transgranular Penetration With Iron-rich Areas. 590x.

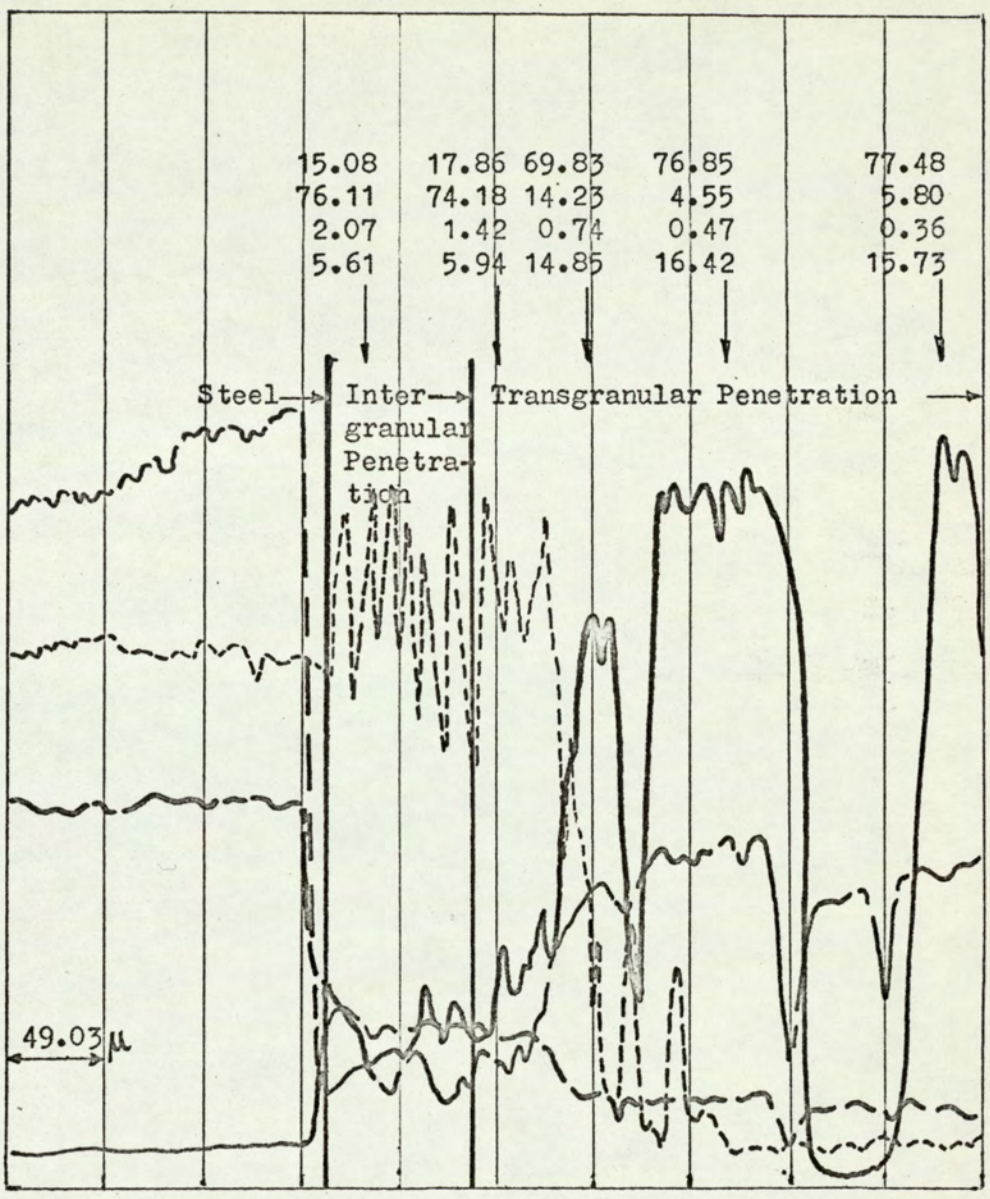

Fig.28 Analysis Of A Corroded Couple After Exposure At 650°C.

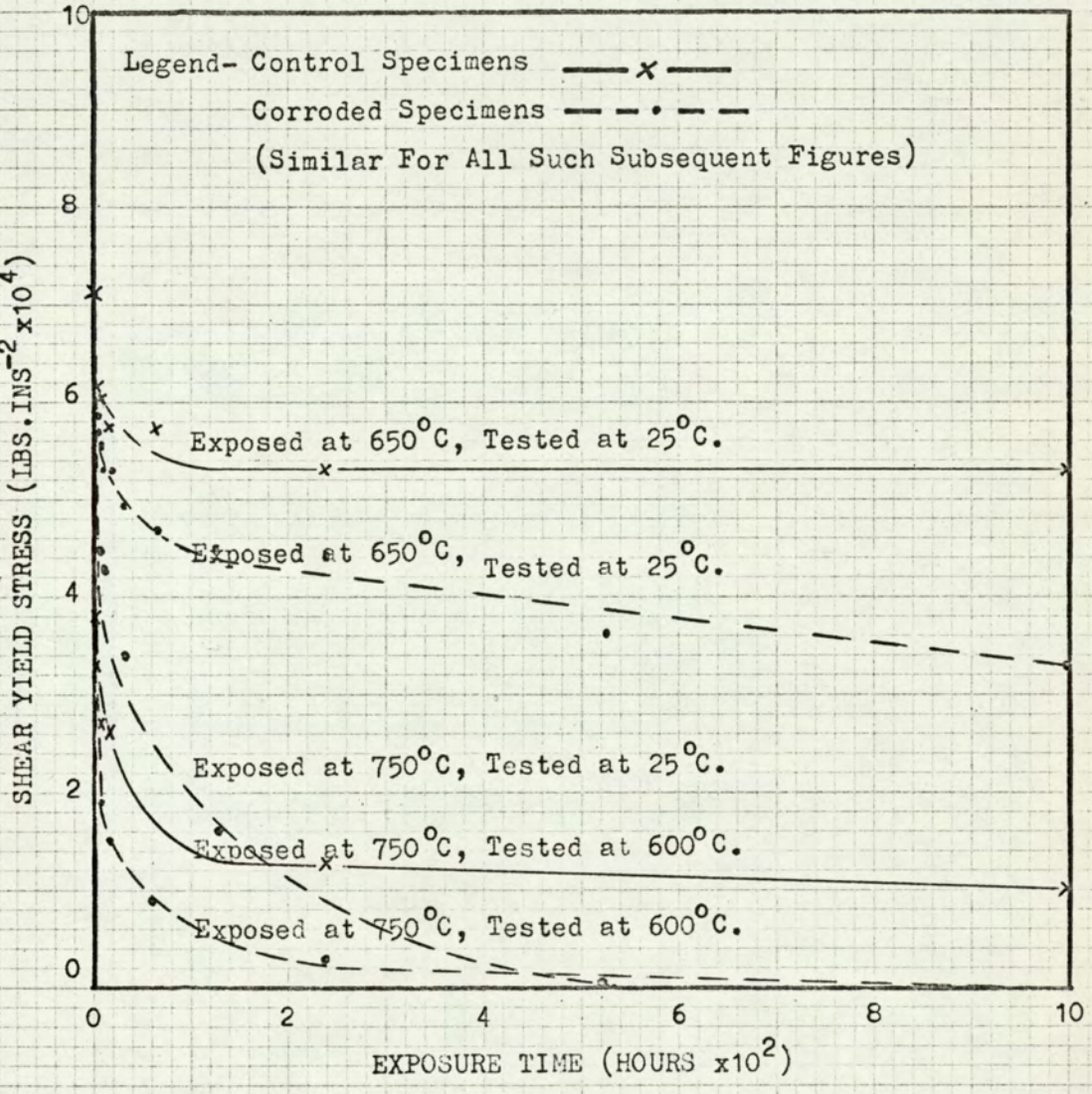

Fig.29 The Shear Stress At Yield As A Function Of Time At Constant Temperature.

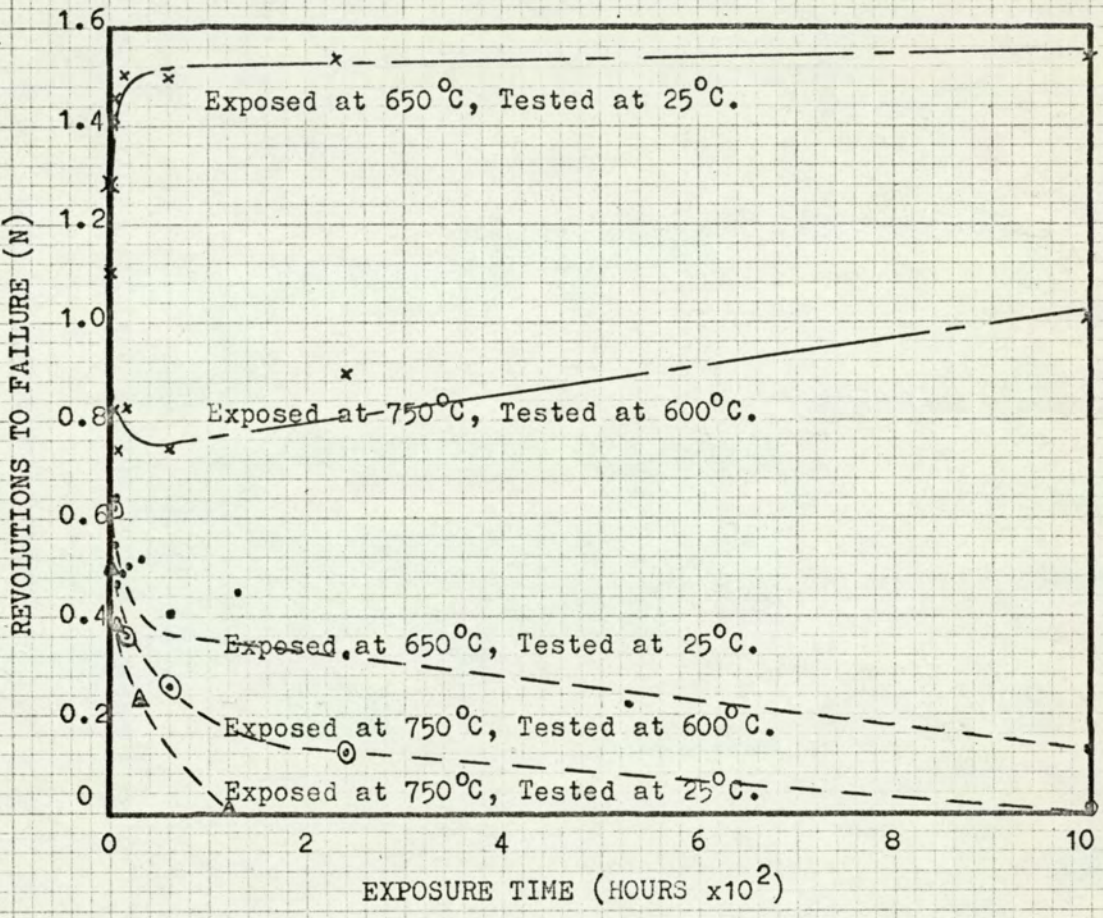

Fig.30 The Number Of Revolutions To Failure As A Function Of Exposure Time At Constant Temperature.

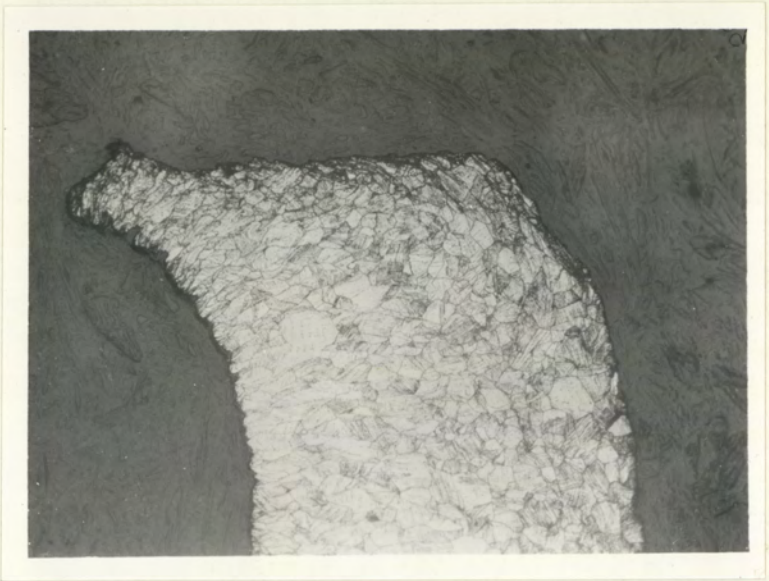

Fig.31 Shear Type Of Fracture Shown By Torsion Testing At 25°C. Longitudinal Section. Etched Electrolytic 10 wt % Oxalic Acid. 100x.

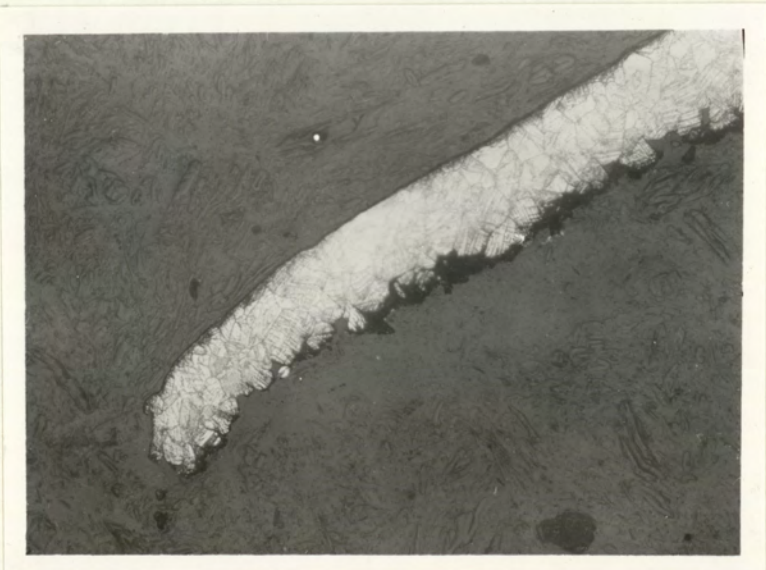

Fig.32 Fracture Of A Corroded Torsion Test Specimen Showing Tearing After Testing At 600°C. Longitudinal Section. Etched Electrolytic 10 wt % Oxalic Acid.

a) Control Specimen. Exposed At 650°C, Tested At 25°C. Cross-section Of Fractured Tube. 25x.

b) As a) 1,275x.

c) Control Specimen. Exposed At 750°C, Tested At 600°C. 6,000x.

Fig.33 Scanning Electron Micrographs Of Torsion Test Specimens With Ductile Fractures.

Fig.34 Torsion Test Specimen Corroded At 650°C For 127 Hours, Tested At 25°C. Shows Brittleness In Corroded Area. Scanning Electron Micrograph 55x.

Fig.35 Torsion Test Specimen Corroded At 750°C For 32 Hours, Tested At 25°C. Illustrates Cleavage In Remaining Te Crystals. Scanning Electron Micrograph 60x.

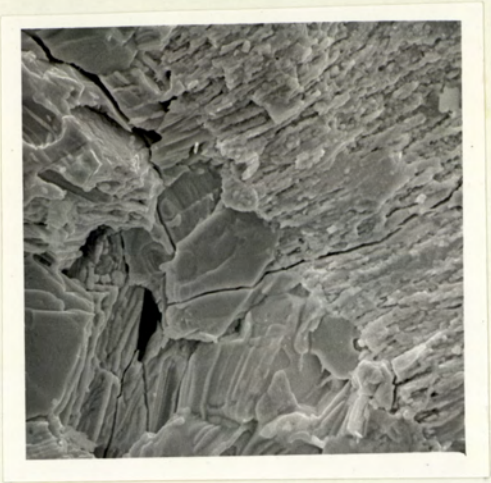

Fig.36 Torsion Test Specimen Corroded At 750°C For 64 Hours, Tested At 600°C. Illustrates Crack Initiation In Te Crystals. Scanning Electron Micrograph 1,175x.

Fig.37 As Above Showing Fracture From The Bore To The Outside Wall Of The Alloy Tube Resulting In Failure. Scanning Electron Micrograph 24x.

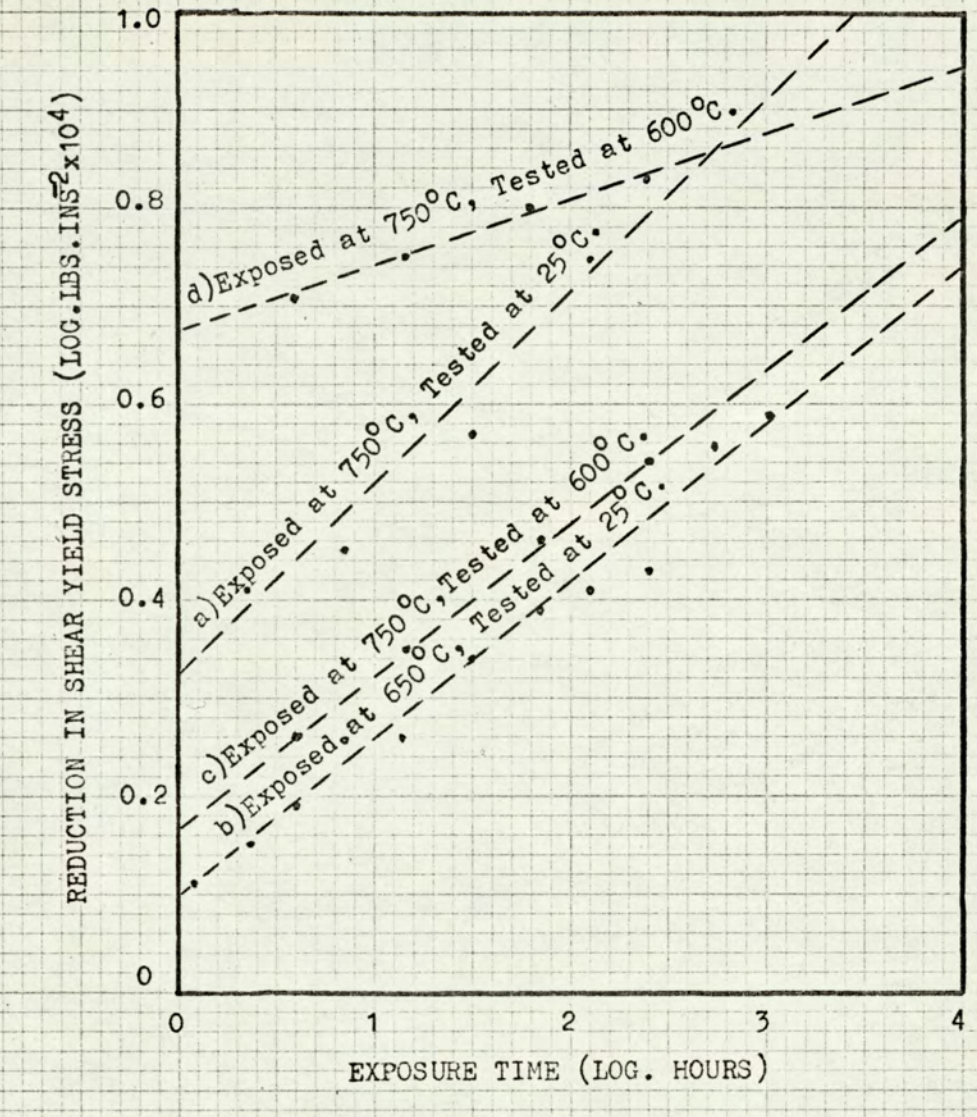

Fig.38 The Reduction In Shear Stress At Yield As A Logarithmic Function Of Exposure Time At Constant Temperature.

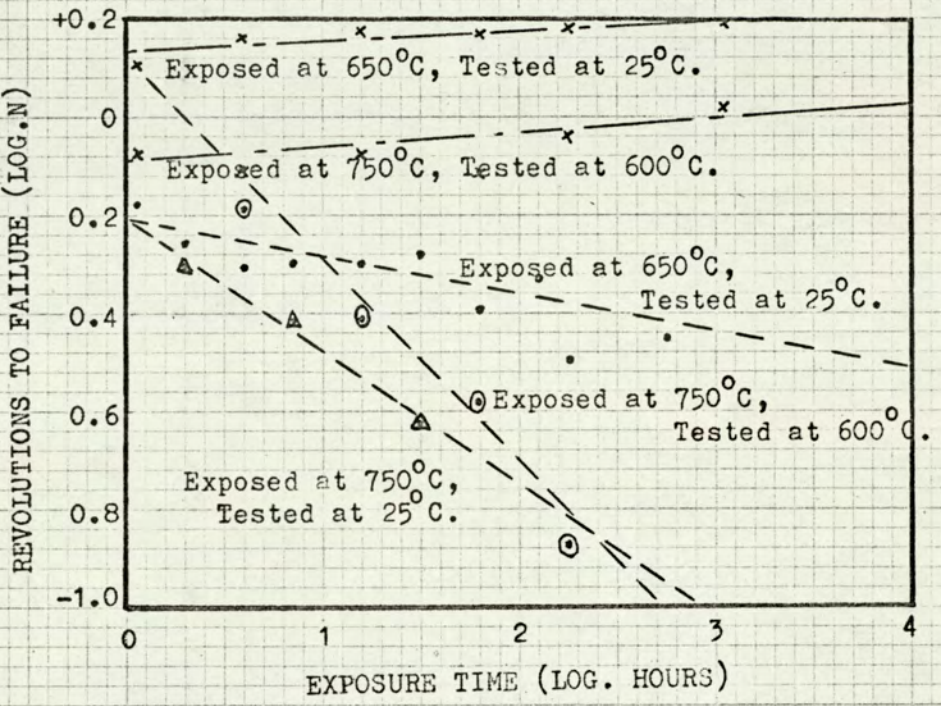

Fig.39 The Number Of Revolutions To Failure As A Logarithmic Function Of Exposure At Constant Temperature.

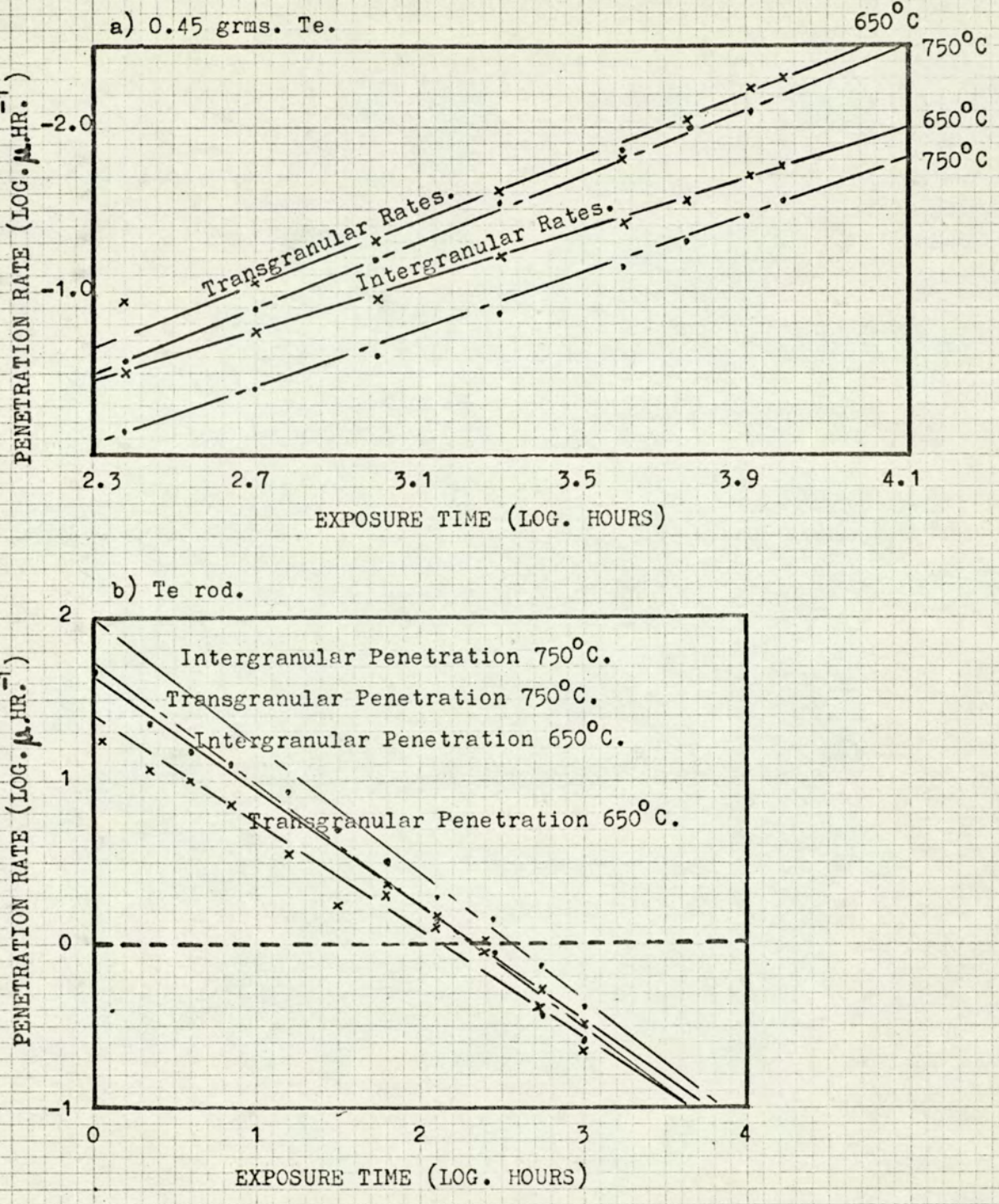

Fig.40a) and b) The Penetration Rate As A Logarithmic Function Of The Exposure Time At 650°C And 750°C.